UNIVERSITY OF TWENTE.

Faculty of Engineering Technology,
Chair of Engineering Fluid Dynamics

Optimizing Geometric Parameters of a Coaxial Nozzle for Direct Bubble Writing

E.R. Zuiderduin

M.Sc. Thesis
July 2019

Document No.
EFD-312
Provisory exam committee:
prof. dr. ir. C.H. Venner (Chairman)
dr. ir. C.W. Visser (Supervisor)
dr. J. Jiang (Internal member)
prof. dr. ir. J.H. Snoeijer (External member)

Faculty of Engineering Technology
Chair of Engineering Fluid Dynamics
University of Twente
P.O. Box 217
7500 AE Enschede
The Netherlands

Preface

This thesis is written to finalize my Master in Mechanical Engineering at the University of Twente. This thesis would not have been the same and this period would not have been as enjoyable without some people. First and foremost, I would like to thank my supervisor Claas Willem Visser. Starting from the first conversation, his enthusiasm about his projects and appreciation for performed work have never dropped and always acted infectious. It was a pleasure working with you and I hope to continue to do so for some time.

Jieke Jiang, Gary Shae and Martin Klein Schaarsberg have helped me by asking questions and giving inspiration and advice during our weekly meetings. The results of this thesis would not be the same without this and I am very grateful for this.

Experimental research is not possible without support from the lab technicians, so thank you Walter Lette and Steven Wanrooij for helping with designing, building and teaching.

Finally I wish to thank my girlfriend, friends and family for always being interested and supportive. Thank you!

Abstract

Cellular materials such as foams appear widely in nature and are manufactured on a large scale by man. Solid foam structures with locally controllable density, pore size and interconnectivity of cells allow for high performance acoustic structures and gradient based tissue scaffolding which could accurately mimic a native tissue architecture. However, conventional production methods are unable to produce these tunable foams. Direct bubble writing is a novel foam production platform (unpublished) on which already foam structures have been produced. This report presents (1) the development of a 3D foam printer and (2) a study on the bubble formation dynamics which is dependent on nozzle geometry and incoming gas and liquid flow.

(1) For the foam 3D printer, requirements have been determined and from several offers, the most complete and cost-effective one was chosen. This included linear actuators, servo drives and a motion controller. The system was then mounted on a granite base which is supported by pneumatic dampeners and an aluminium frame. This system will be used in future research to 3D print foam geometries in programmable shapes. (2) For the study on bubble formation dynamics, core-shell nozzles were designed to create bubbles which constitute the cells in the 3D printed foam. The nozzles were 3D printed which allowed tunable control parameters, including the inner and outer nozzle diameter, outer wall angle and distance from inner to outer nozzle orifices. The nozzles were mounted in a set-up where a range of liquid flow rates and gas pressures were supplied and the resulting ejection phase was recorded in order to compare the nozzles. A large distance between inner and outer nozzle does not result in gas encapsulation and a small distance was not able due to the production method. Stable ejection in the form of connected bubble trains and multidisperse bubbles which can be used for direct bubble writing were obtained with an intermediate distance between the inner and outer nozzle. A small outer nozzle diameter showed jetting for higher liquid flow rate at intermediate gas pressure where intermediate outer nozzle diameters showed bubble formation and for even larger outer nozzle diameters the formed bubbles attached to the nozzle until the cluster of bubbles became too large and separated itself from the nozzle. In order to compare a large range of nozzle geometries, a model for bubble transition pressure was used to compare dimensionless results. The results for all types of nozzle geometries correspond well with each other and distinct ejection regimes can be observed. The transition from dripping to jetting due to an increasing effect of inertial forces which is modelled with the Weber number corresponds well with literature. The pressure at which gas is introduced in the ejection corresponds well with the transition pressure model as proposed by S. Coco and C.W. Visser. Using the dimensionless results and the ejection regimes an estimation can be made for the required liquid ejection velocity and gas pressure when using a new nozzle geometry and liquid in order to produce monodisperse bubbles.

Contents

Chapter 1

Introduction

Today's engineering challenges require the optimization of a structure's stiffness, weight and other properties. These are expected to be available in large-scale tunable materials such as foams. As a result, material engineering aims to find new materials and new production methods.
Solid foams exhibit large surface-to-volume ratios, low density and interconnectivity of cells causing them to have unique mechanical, acoustic and thermal properties. They are therefore widely used as thermal insulators, acoustic dampeners and shock absorbers. Conventional production methods are only able to produce bulk material with no local control over resulting density, pore sizes and interconnectivity of cells [1], [2]. Figure 1.1a shows examples of monodisperse foam and a polydisperse foam which can be produced using existing production methods. The polydisperse foam shows irregular diameter cells at the center and smaller diameter cells at the walls. This is due to the skin layer formation on the surface but there is little control over this happening [3].
In nature anisotropic structures are observed which allow for a high level of mechanical efficiency, meaning mechanical performance per unit mass. Palm and bamboo show a fibre-reinforced cross-section where there is a gradient of fibre density and elastic modulus which is higher near the periphery. This allows these stems to grow long and slender while having a high flexural rigidity with minimal resources [4], [5] as can be seen in figure 1.1b.
High performance acoustic foams could benefit from incorporating gradients as was shown by additively manufactured acoustic structures [6]. Also in the field of tissue engineering a hierarchical foam could have high potential [7], [8]. The spatial arrangement of tissue scaffolding can develop cells to form functional tissue as seen in bone tissue [9]. With current additive manufacturing techniques there are still limitations to the complexity of the scaffolding [10].

The process direct bubble writing as shown in figure 1.2 aims to solve the limitations of conventional polymer foam production methods. This process was developed at the Lewis Lab at Harvard University, by Dr. Claas Willem Visser and others. It allows the rapid manufacturing of polymer foams which can incorporate gradients in density, allow for local interconnectivity of cells and allows for the printing of programmable shapes. A coaxial nozzle rapidly forms bubbles of a gas-filled photopolymerizable ink shell which are solidified in-air with UV light. These bubbles are deposited on a substrate and an agglomeration of solidified bubbles forms a foam. The coaxial nozzle is mounted on 3-dimensional actuation stages in order to produce 3-dimensional parts similar to additive manufacturing techniques like fused deposition modelling (FDM) or Directed energy deposition (DED). The previous research was done using a single nozzle design with which already some insight was gained on the effect of fluid flow rate and applied gas pressure and the resulting phase, bubble diameter and density. In order to be able to produce foams at different length scales the input flow can be adjusted to a certain extent. Changing the nozzle geometry is also expected to have an effect on the

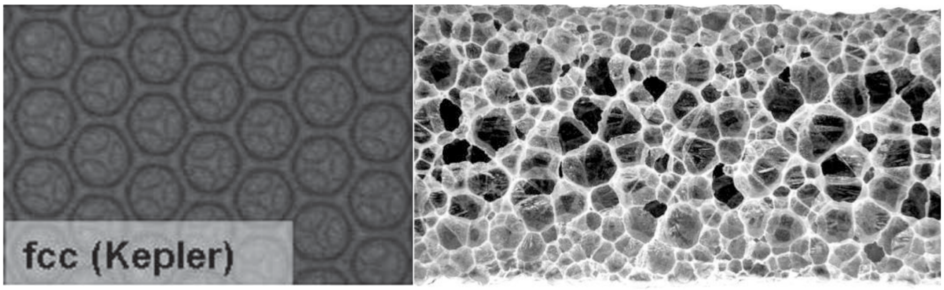

(a)

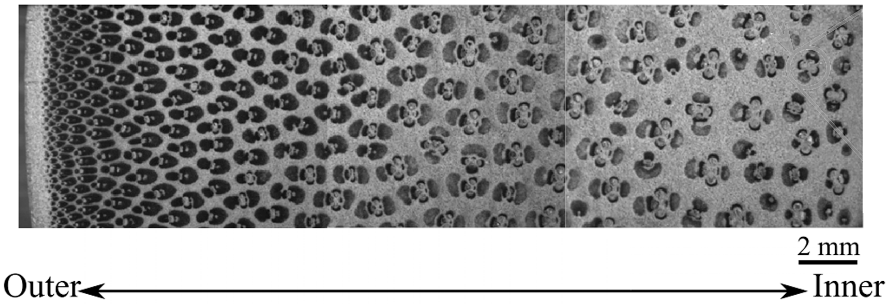

(b)

Figure 1.1: a) Man-made monodisperse bubbles [11] and polydisperse PE foam sheet [3]. b) The hierarchical structure of bamboo [5].

resulting phases at different ink flow rate and gas pressure. In my research the effect of changing the nozzle geometry is investigated and a dimensionless analysis is done in order to predict the relevant ink flow rate and gas pressure for varying nozzle length scales. In addition, a tailored 3D stage was developed in the lab at the University of Twente to continue the research on direct bubble writing.

1.1 Objectives

1. Design a custom set-up as a platform for Direct Bubble Writing
2. Fabricate coaxial nozzles in tunable designs
3. Investigate the ejection phases from the coaxial nozzles with varying ink flow rate, gas pressure and nozzle dimensions
4. Investigate dimensionless results for up- and down scaling of the process

1.2 Outline

The thesis contains three main chapters followed by the concluding chapter. Chapter 2 briefly reviews previous work on the process of direct bubble writing which is relevant to this thesis. This work mentions high speed imaging analyses of nozzle ejection and the influence of viscosity on the resulting phase and a proposed model for gas introduction in the ejection.
Chapter 3 starts by introducing the required set-up and some verification on the bending and vibration of the system. The chapter continues with verification of the repeatability of the 3d printed nozzles. The experimental set-up is then introduced. Chapter 4 shows the parameter investigation

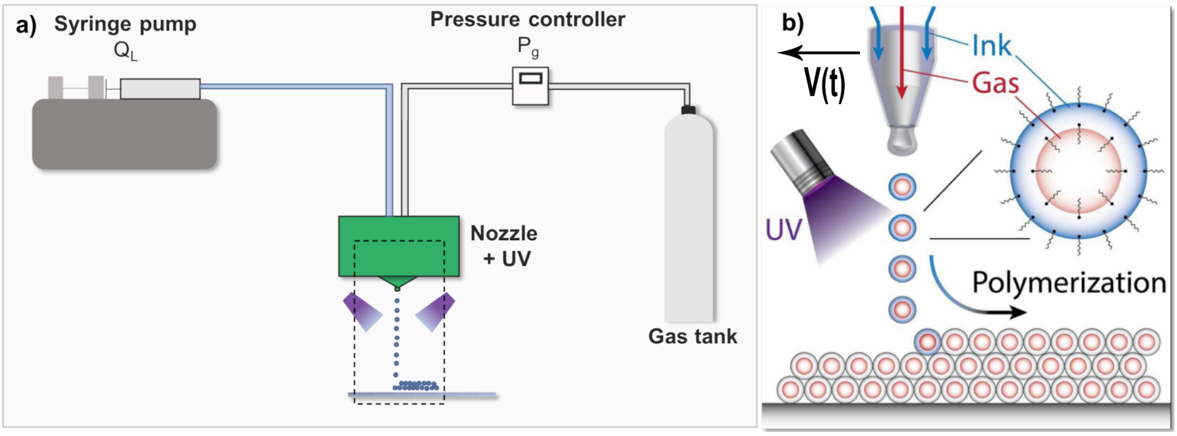

Figure 1.2: Schematic overview of the direct bubble writing process [copied from [12]]. a) Precise control over liquid and gas supply is achieved by a syringe pump and pressure controller, respectively. The dashed lines indicate where these fluid flows come together in the nozzle which is further shown in b) The liquid and gas flow meet in the coaxial nozzle and form a stream of bubbles which is polymerized with UV radiation and deposited on a substrate. Nozzle actuation allows for programmable shapes.

of the nozzles. The results are then visualized in different ways and compared to literature.
The last chapter contains the conclusions from this thesis and the recommendations for further research.

Chapter 2

Previous work

The feasibility of direct bubble writing was shown in previous work by Dr. Claas Willem Visser. The ejection phase as a function of fluid flow rate and gas pressure was investigated as shown in figure 2.1. For low pressure, jetting is observed. When increasing this pressure, the ejection transitions to bubbles with constant diameter. For higher applied gas pressure the process becomes more unstable and bubbles of multiple diameters are formed. For even higher pressure the bubbles become even more unstable and burst upon ejection from the nozzle and a spray is formed. This knowledge was used to produce foams at varying gas pressures in order to investigate the foam's density. The foam's density as a function of pressure and close up images of monodisperse and bidisperse foams are shown in figure 2.2.

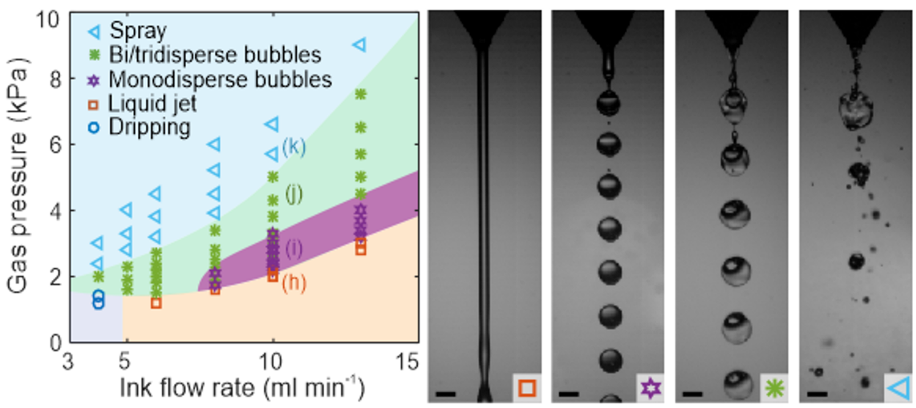

Figure 2.1: Phase diagram mapping the ejection phase for varying fluid flow rate and gas pressure. The markers correspond to the images on the right showing the different ejection phases. [Property of Dr. Visser].

The nozzle was mounted on an XYZ-stage which allowed for the production of programmable shapes as shown in figure 2.3.

Overall, the process direct bubble writing has been shown to be able to produce polymer foams at varying densities, electrical properties and free-form geometries. This allowed for the fabrication of custom foams with a programmable deformation profile and foams for pressure sensing applications.

However, in order to understand more about the bubble forming process and resulting foams, additional research was carried out. S. Coco continued the research on this process, resulting in the following improvements and understanding [12]:

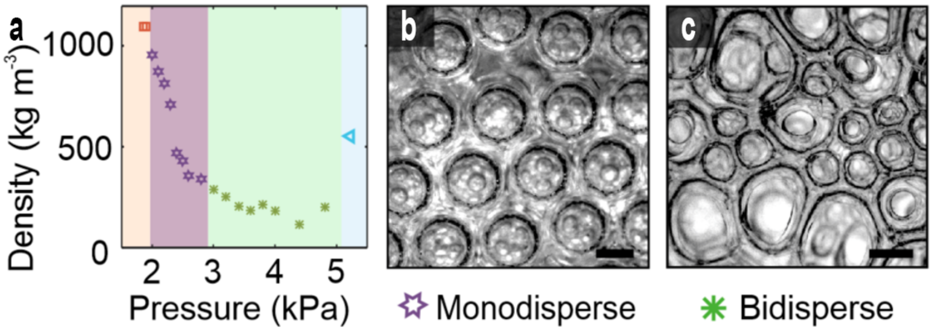

Figure 2.2: a) The density as a function of applied gas pressure. b) For lower applied pressures monodisperse foams are formed. c) At intermediate pressures bidisperse foams are formed. [Property of Dr. Visser].

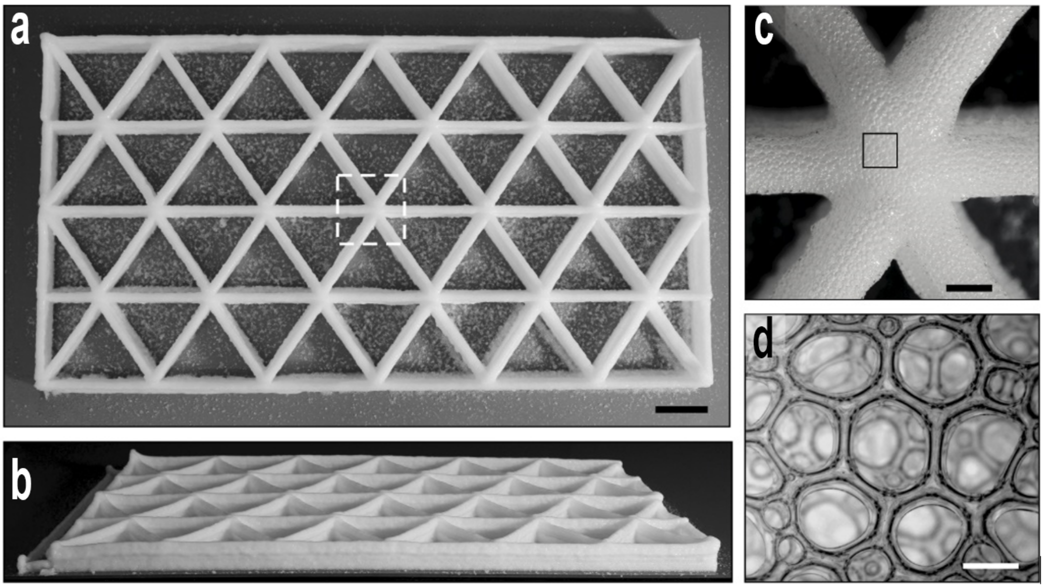

Figure 2.3: a,b) Large scale rectangle with triangular infill. c) View of the connections with d) close-up image of the small-scale architecture. [Property of Dr. Visser]. Scale bars: (a) 50 mm; (c) 5 mm ; (d) 0.5 mm.

2.1 Volumetric flow rate and foam density analysis from high speed imaging of ejecting bubble train

Consecutive images from high speed footage of the bubbles ejecting from the nozzle were analyzed using image postprocessing as can be seen in 2.4. Using the images and the camera frame rate the bubble diameter, ejecting velocity, distance between bubbles and thus the volumetric flow rate were found. The results show an increasing diameter and the transition from monodisperse bubbles to polydisperse bubbles for increasing pressure with constant ink flow rate as shown in figure 2.5a. The bubble velocity also significantly increases from 1 m/s to 2.7 m/s for increasing pressure as shown in figure 2.5b.

A total gas and liquid flow rate of 80 mL/min was achieved which confirms high throughput of the process. With the used nozzle design, the large structure of dimensions 60x40x3 cm^3 in figure 2.3a can be made in 22 minutes.

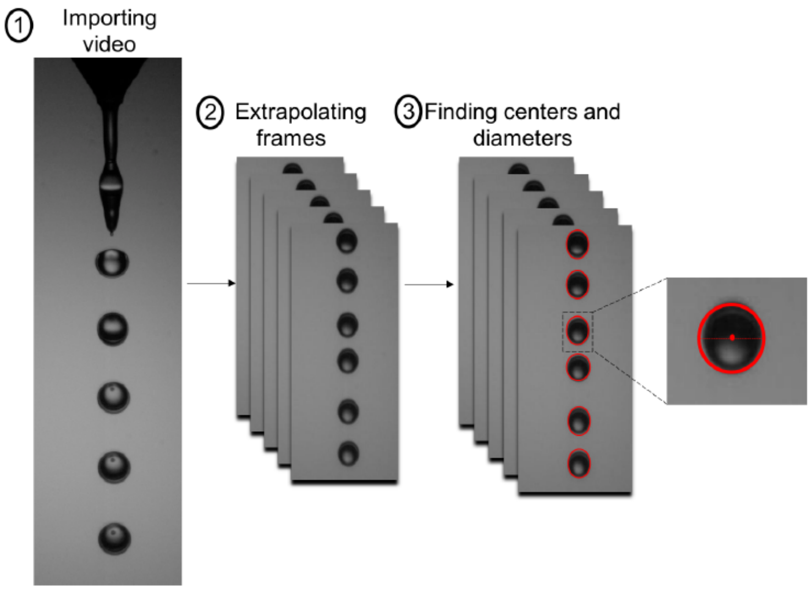

Figure 2.4: Image post-processing steps. First the videos are imported and the individual frames are extracted. The relevant region of the images is selected and enhanced. Some algorithms then were used in order to recognize the bubbles, diameters and the center positions. Figure copied from [12].

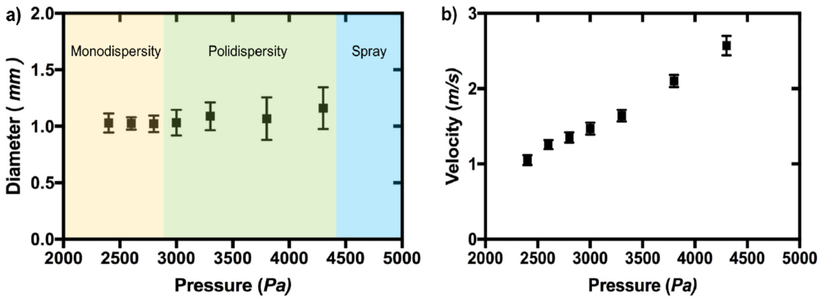

Figure 2.5: a) The resulting bubble diameter as a function of applied gas pressure. b) The measured velocity as a function of applied gas pressure. Figure copied from [12].

2.2 The influence of liquid viscosity on the bubble formation transition

It was noticed that a high viscosity fluid required a higher pressure in order to result in the same ejection regime compared to a lower viscosity fluid. Several fluids were prepared with a viscosity ranging from 1 Mpa.s to 300 Mpa.s. These were ejected from the nozzle with different ink flow rates and pressures. The transition pressure at which bubbles were formed was used to build a theoretical model. This transition can be seen in figure 2.6. The model takes three components of mechanical stresses into account which are capillary pressure 2.1a, dynamic pressure 2.1b and the pressure drop due to friction 2.1c. The summation of these pressures gives a reliable indication of the transition pressure from pure liquid ejection to gas encapsulation in the liquid as shown in figure 2.7. In this figure the markers represent the observed transition pressures for liquids with varying visosities. The continuous lines are the pressures resulting from the theoretical model which correspond well with the experiments.

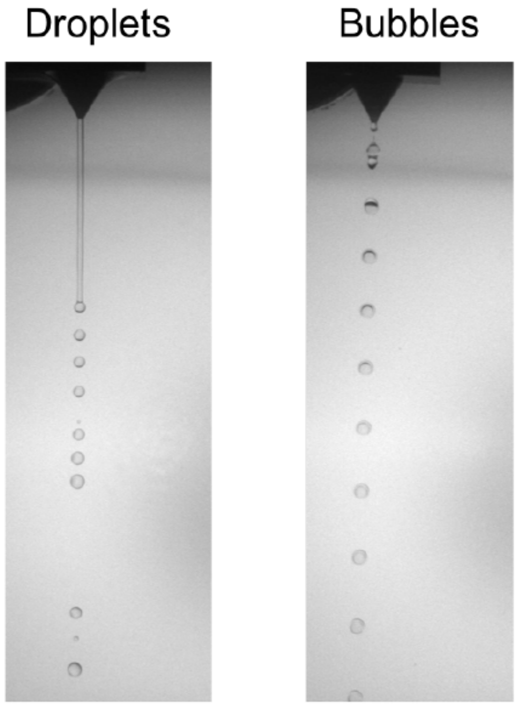

Figure 2.6: Images showing ejection of purely liquid phase on the left and bubbles in the right figure. Figure copied from [12].

$$\Delta P_{Laplace} = \frac{2\gamma}{R} \tag{2.1a}$$

$$\Delta P_{Bernouilli} = \rho_L v^2 \tag{2.1b}$$

$$\Delta P_{Darcy-Weisbach} = \frac{128\mu Q_L L_t}{\pi D_t^4} \tag{2.1c}$$

$$P_{tot} = \Delta P_{Laplace} + \Delta P_{Bernouilli} + \Delta P_{Darcy-Weisbach} \tag{2.1d}$$

In these equations, γ is the surface tension of the fluid in [mN/m], R is the radius of the inner nozzle in [m], rho_L is the density of the liquid in [kg/m^3], v is the velocity of the liquid in [m/s], μ is the kinematic viscosity of the liquid in [cP], Q_L is the flow rate of the liquid in [m^3/s], L_t is the distance between inner nozzle and outer nozzle in [m] and D_t is the diameter of the outer nozzle in [m].

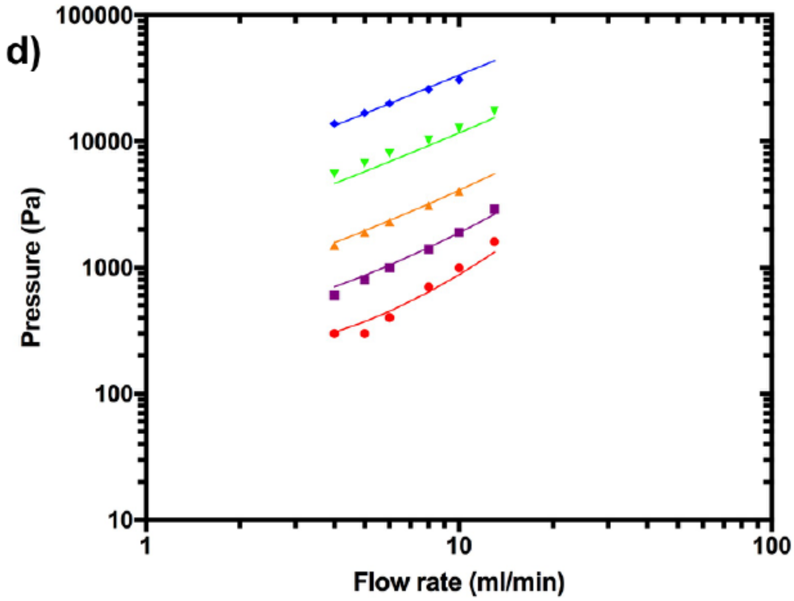

Figure 2.7: The transition pressure for increasing viscosity. The different colors represent liquids with viscosities ranging from 1 to 300 cP. For a certain flow rate, the gas pressure was increased until gas was introduced in the ejecting phase. This transition pressure is indicated with the markers. With equation 2.1 the transition pressure is calculated for changing flow rate and this is indicated by the continuous line. Figure copied from [12].

Chapter 3

Set-up

The previously mentioned research was done at the Lewis Lab at Harvard University. In order to be able to print foams at the University of Twente a tailored setup was developed as part of this graduation assignment. The bubble forming process requires a nozzle design (chapter 3.3), the supply of liquid and gas (3.4), UV radiation (chapter C) and some mounting structure. The process itself requires some form of actuation in order to fabricate foam in programmable geometries similar to various extrusion based 3d printing process. This actuation is required in three dimensions which are named the x- and y-axis for the horizontal plane and the z-axis for the vertical component. Each linear actuation requires a motor in able for the end effector to move along a certain axis and some sort of control and feedback loop in order to accurately describe the programmed profile. The following section focuses on the system which enables the xyz motion.

3.1 Requirements

A printed foam geometry will be built in a layer-based approach. The geometry is divided in slices which are printed sequentially. Each layer consists of a path where it deposits foam bubbles in a continuous manner. This way the entire layer shape is laid down. After each layer the build platform or the print head changes its height to account for the change in distance between the nozzle and the top layer of the foam product. Then a new layer can be deposited.

In order to accurately produce the programmed shape, the velocities and accelerations of the horizontal axes are important. If the print head is actuated too slowly, the deposited bubbles will cluster together and a thick line is formed. When this velocity is increased, the width of the formed line decreases until at a certain velocity a single line of bubbles is formed as in figure 3.1.

Increasing the velocity further would cause the individual bubbles to no longer be connected to neighbouring bubbles in the line. The process might be up-scaled which induces a larger volume flow which might require a higher velocity in order to get a single line of bubbles. The required velocity is therefore set to be 500 mm/s.

Since the printing process is continuous, the velocity of the print head has to be maintained. This is important when the direction of the print head is changed. Changing direction will require deceleration in one direction and acceleration in another direction. If a perpendicular angle is attempted, this will require the print head to first decelerate to a stop in one direction and then accelerate in the other direction. The decrease in velocity will cause many bubbles to cluster in the corner and an inaccurate corner is the result. This can be solved by corner rounding. In a round corner the velocity of the print head is decreased gradually in one direction while the velocity in the other direction is increased gradually. The radius of the corner which can be turned at a steady velocity is dependent on

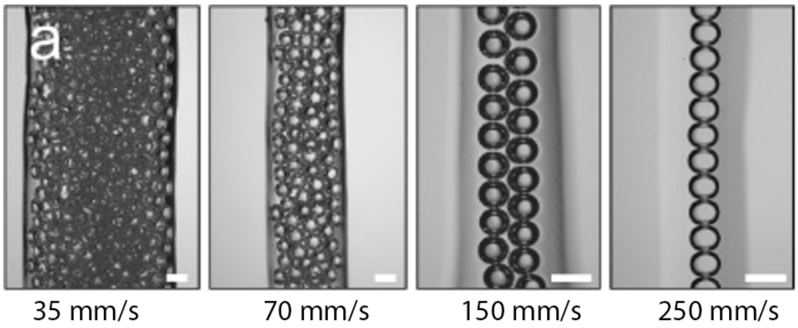

Figure 3.1: Increasing print head velocity and resulting filament width. Scale bar: 1 mm [Property of Dr. Visser].

the acceleration the set-up is capable of and the velocity at which the print head is moving. A lower velocity means that the process of acceleration and deceleration can be done in a shorter amount of time and a smaller radius is possible. The same goes for a higher possible acceleration. This is visualized in figure 3.2. For an equal velocity, doubling the maximum acceleration will half the radius and also the cycle time. For the set-up, an acceleration of 10 m/s^2 is considered sufficient as it leads to a minimal corner radius of 25 mm while travelling a constant 500 mm/s. A lower velocity will allow for a smaller radius but the previously mentioned requirement of 500 mm/s is taken to give an idea about the worst case scenario.

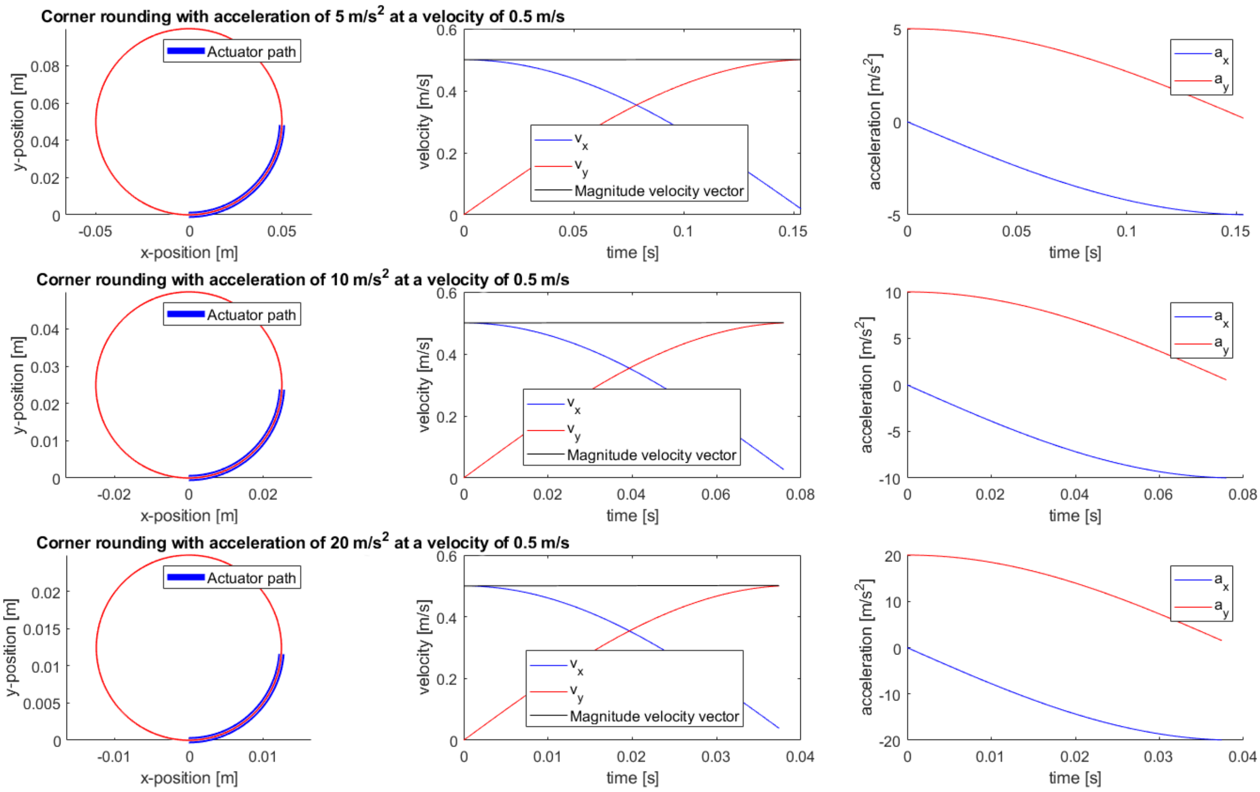

Figure 3.2: Corner rounding at different values for acceleration and resulting cycle time and radius.

Another requirement is the accuracy the finished system. Since the machine will be used for printing layers on top each other, the repeatability is set as the important measure of accuracy. When the print head is actuated along a path it is important that the actual path of each layer corresponds well with the path of the previous layers in order to produce an accurate part. The absolute accuracy of each point is more difficult to achieve because of factors like deflection of the y-axis due to gravity, bending of the y-axis due to acceleration, both of which will be different over the print volume. These can be accounted for but this will take a lot more computing force and measurements.

The print volume determines the required lengths of the linear axes and this has direct influence on the actuated mass of the system. The mass of the print head is also taken into account.

The resulting requirements are shown in table 3.1. Available consumer 3d printing platforms generally allow for lower velocity, lower acceleration and lower accuracy. A popular 3d printing process is FDM for which many affordable solutions are available. The plastic extrusion rate is usually limited (with an exception for large diameter nozzle systems with large layer height resulting in a lower resolution but high volume throughput). Usual printing velocities range from 50-70 mm/s with an acceleration of 0.5 m/s^2. The outer perimeter is usually printed slower in order to decrease vibrations and increase the visual results of the print. Movements that don't influence the resulting printing accuracy like the travel speed are commonly set up to 180 mm/s and with a higher acceleration up to 2 m/s^2 [13]. The supporting structures are not suited for higher velocities and accelerations and will cause substantial vibrations and inaccuracies. Therefore several companies have been contacted in order to arrive at a set-up capable of handling the required velocities and accelerations with the desired accuracy. This is further discussed in appendix B.

3.2 Linear axes set-up verification

The reulting set-up is shown in figure 3.3a. Three linear actuators are mounted in series so in consecutive order with each actuator allowing one translational degree of freedom corresponding to the axes in figure 3.3a. Each actuator consists of a moving part(the carriage) and a static part(the stator). The X stator is mounted on the granite table and the X carriage amounts for the movement in the X direction. The Y stator is mounted on the carriage of the X axis and movement of the X carriage thus also induces movement of the Y stator and carriage. The Y carriage allows for movement in the Y direction. The Z stator is mounted on the Y carriage and X-Y movement of Z stator and carriage are possible with motion of the X and Y carriages. The Z carriage allows for movement in the Z direction. An appliance can be mounted on the Z carriage so that it can move in three directions. In order to have a sufficiently stiff system, the Y axis has been equipped with additional mounting structures as can be seen in figure 3.4. This increases the mass of the system which in turn has detrimental effects on vibration since a higher mass with similar stiffness lowers the eigenfrequencies of a system [14]. Another frequently used design is the so-called H-bridge design which is a lot stiffer since it is supported at two sides. This does require that both sides are actuated with an active control loop in order to prevent binding issues. The chosen set-up in appendix B is less expensive since it doesn't require an additional actuated axis but it needs to be verified whether

Table 3.1: Listed requirements for the proposed system.

Requirement	**Value**	**Unit**
Velocity	500	mm/s
Acceleration	10	m/s^2
Print Volume[X,Y,Z]	[500,500,50]	mm
Accuracy[repeatability]	10	μm
Print head	1-3	kg

the deflection and vibrations of the system are within range so they do not conflict with the system requirements.

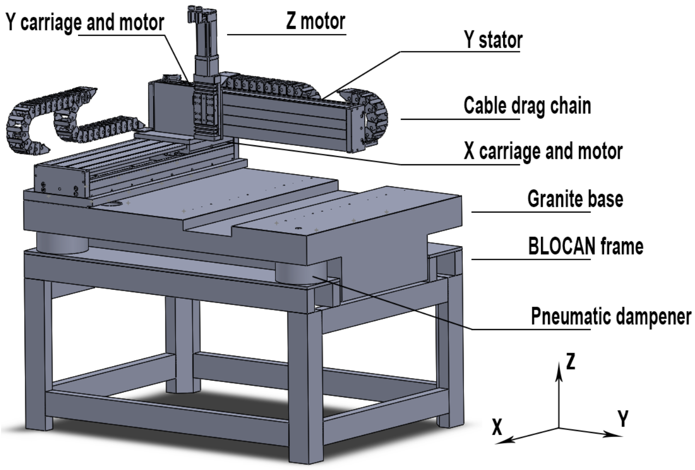

(a)

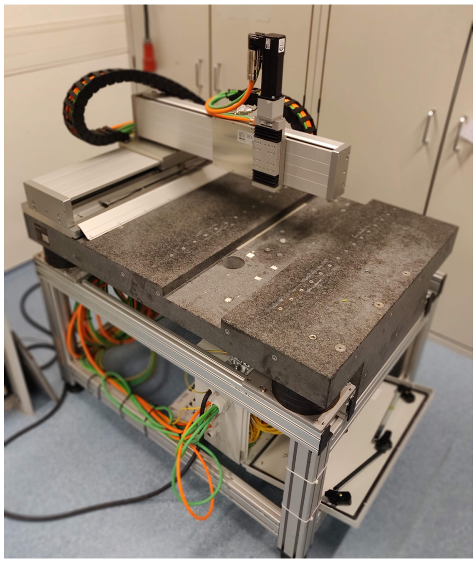

(b)

Figure 3.3: (a) Model of the linear actuators and the base (b) Photograph of the set-up in the laboratory.

3.2.1 Y-axis deflection due to gravity

The design in figure 3.3a shows that the Y-axis is fixed on one side and left hanging free on the other. The mass of the actuator arm and the attached mass of the carriage with Z actuator taken as a point load will cause the arm to bend under influence of gravity. The equations which describe these two load cases are equations 3.1 and 3.2.

$$\delta_{uniform} = \frac{qL^4}{8EI} \tag{3.1}$$

$$\delta_{point} = \frac{Py^2}{6EI}(3L - y) \tag{3.2}$$

In these equations, q is the distributed load [N/mm], L is the actuator arm length [mm], E is the Young's Modulus [N/mm^2], I is the area moment of inertia [mm^4], P is the gravitational force due to the carriage taken as a point mass [N], y is the distance from the point on which the force is acting to the fixed end [mm]. For small deformations, the individual effects of both loads on the structure geometry is small so can be neglected. For these small elastic deformations conforming Hooke's law these contributions to the deformation can then be added in order to find the system's response to the simultaneous load case. $\delta_{total} = \delta_{uniform} + \delta_{point}$. The mass of the X axis moving mass(X carriage, Y stator, Y carriage, Z actuator and both cable drag chains) and Y moving mass(Y carriage, Z actuator and cable chain) are known to be 32 kg and 12 kg, respectively. These can be used as the applied loads with the gravitational constant. The X carriage, mounting structure and cable chain are expected to have a significant weight but the exact weight is unknown. The total weight is therefore used of X axis moving mass and Y axis moving mass are therefore used for the applied loads to give insight in the worst-case scenario. The Y-axis length is 680 mm and the material is assumed to be steel. This material has a higher Young's modulus compared to aluminium, but the influence of this choice is later mentioned. The cross section is assumed to be a rectangular tube with a height, h of 135 mm and a width, w of 70 mm which is derived from the supplied model. The wall thickness, t is taken as 5 mm. This profile is shown in figure 3.5. The location y at which the print head is positioned is taken as 600 mm from the fixed end. The area moment of inertia of a rectangular tube can be calculated as:

$$
\begin{aligned}
I_{solid} &= \frac{1}{12} w h^3 \\
I_{inner} &= \frac{1}{12} (w - 2 \cdot t)(h - 2 \cdot t)^3 \\
I_{tube} &= I_{solid} - I_{inner}
\end{aligned}
\tag{3.3}
$$

Filling in equations 3.1 and 3.2 results in 8.2 μm and 10.8 μm, respectively. To verify this a simulation has been done which uses the same cross section as the available model. This has been done using Autodesk simulation software. A cross section of the Y-axis is shown in figure 3.4. A perpendicular view of the cross section of the supplied model and the derived geometry are shown in figure 3.5b and 3.5c. In figure 3.5d it can be seen that the deflection due to gravity of the actuator arm is in the same order of magnitude as the calculated deflection of the rectangular tube. The deflection of the actuator arm at rest when the print head is moved 500 mm towards the fixed end is calculated as 8.6 μm so the effect of the point mass is negligible in this situation. This deviation in height of about 10 μm is not critical for the functioning as actuation for Direct Bubble Writing. Even a process such as Fused Filament Fabrication which deposits material directly onto a surface can function with a build surface height deviation of $\pm$ 0.03 mm, so fabrication processes other than Direct Bubble Writing can also be mounted on this machine. The material which was used in both the simulation and the deflection calculation was steel. It is also likely that aluminium was used which is a lighter non-magnetic material. Using an aluminium profile in the calculations causes a threefold increase in the deflection since the Young's modulus of aluminium is three times lower compared to steel. The X axis moving mass was given as 32 kg, but this mass also includes the mass of the X carriage and the mounting structure and the cable drag chain along the X-axis. These masses are set-up near the applied force of the linear motor and these masses won't cause bending of the Y-axis. Since an accurate weight of the Y stator and carriage are unknown, the deflection calculation and simulation remain more an estimation of the order of magnitude of deflection which is significantly small.

3.2.2 Actuator arm vibration analysis

This axis is clamped on one side on the X carriage which is actuated. The accompanying acceleration and deceleration will induce forces, stresses and therefore bending and vibrations of this Y-axis. The equation of motion for a beam in free vibration is given by equation 3.4 which is derived from the forces and moment balance of a small section of a beam [15]. The deflection $x(y,t)$ is in the direction in which the entire Y-axis is translated, since the clamped end is mounted on the X carriage. The same simplification of the cross section has been done as in the calculation of the deflection in section 3.2.1. The mentioned deformations and directions correspond to the coordinate systems as shown in figures 3.3a and 3.4

$$
\frac{\partial^2}{\partial y^2} \left[EI(y) \frac{\partial^2 x(y,t)}{\partial y^2} \right] = -\rho A(y) \frac{\partial^2 x(y,t)}{\partial t^2} \tag{3.4}
$$

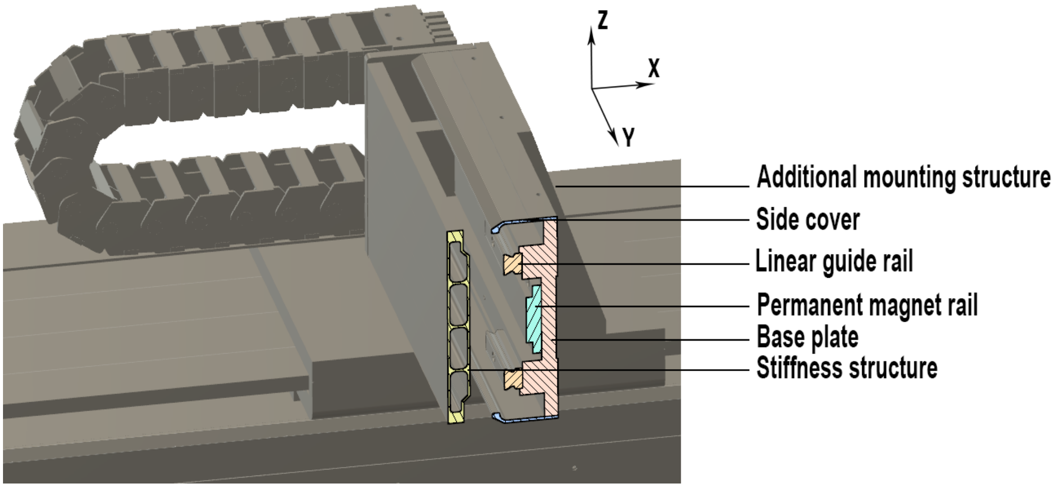

Figure 3.4: Section view of the Y-axis actuator.

This equation can be simplified by assuming a homogeneous beam so the E and I are not position dependent. The cross-sectional area also does not change along the y-axis so is independent of y.

$$EI\frac{\partial^4 x(y,t)}{\partial y^4} = -\rho A\frac{\partial^2 x(y,t)}{\partial t^2} \tag{3.5}$$

The harmonic vibration solution x(y,t) is separable in position y and time t so can be separated as follows in which F(y) is the mode shape T(t) is the time dependent part. Depending on the initial condition T(t) is a combination of a sine and cosine wave with ω as the associated natural frequency. For simplicity a sine wave is considered which leaves:

$$x(y,t) = X(y)T(t) = X(y)\sin\omega t \tag{3.6}$$

The left and right side of equation 3.5 can then be expressed as done in equation 3.7 and 3.8.

$$\frac{\partial^2 x(y,t)}{\partial t^2} = X(y)\frac{d^2\sin\omega t}{dt^2} = -X(y)\omega^2\sin\omega t \tag{3.7}$$

$$EI\frac{\partial^4 x(y,t)}{\partial y^4} = EI\sin\omega t\frac{d^4X(y)}{dy^4} \tag{3.8}$$

Filling these in in equation 3.5 gives:

$$EI\sin\omega t\frac{d^4X(y)}{dy^4} = \rho A X(y)\omega^2\sin\omega t \tag{3.9a}$$

$$\frac{d^4X(y)}{dy^4} = \frac{\rho A\omega^2}{EI}X(y) \tag{3.9b}$$

$$\frac{d^4X(y)}{dy^4} = \beta^4 X(y) \quad \text{with} \quad \beta^4 = \frac{\rho A\omega^2}{EI} \tag{3.9c}$$

$$\frac{d^4X(y)}{dy^4} - \beta^4 X(y) = 0 \tag{3.9d}$$

The standard solution for equation 3.9d is:

$$X(y) = A\sin\beta y + B\sinh\beta y + C\cos\beta y + D\cosh\beta y \tag{3.10}$$

The values for the unknowns can be found by using the boundary conditions. The axis is clamped on one side. There is therefore no deformation on the clamped edge of this axis and the deformation

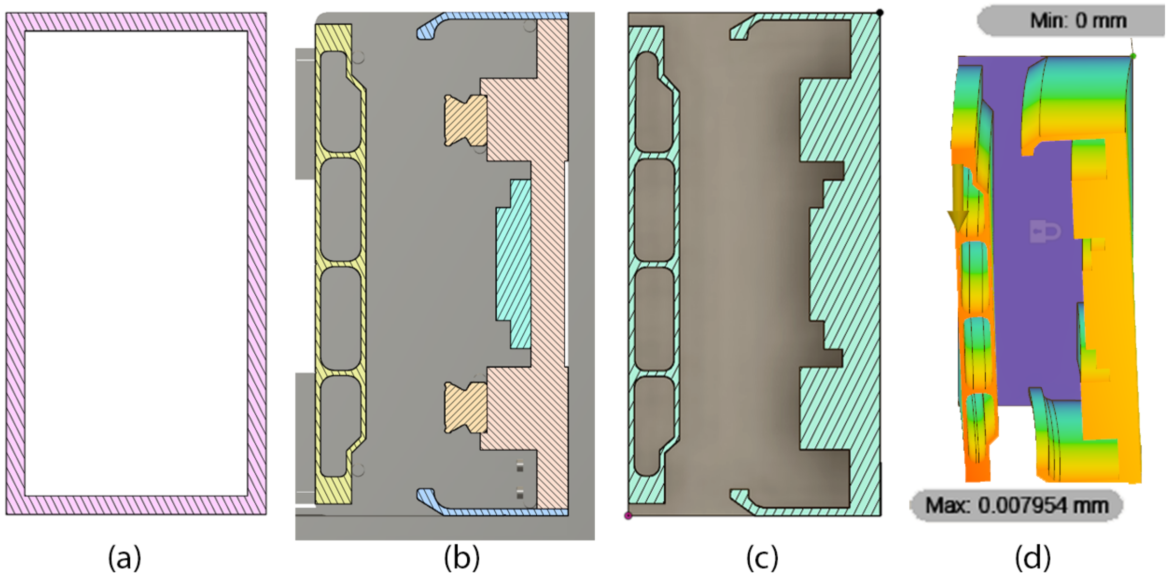

Figure 3.5: Section view used in the calculations and simulations: (a) section view of the rectangular tube used in the deflection and vibration analysis, (b) section view of the Y-axis as supplied by ATB Automation, (c) section view of the modelled geometry used for the deflection and vibration simulation and (d) the results from the simulation showing deflection due to gravity. This is a section of the three dimensional simulated deformation.

angle is also zero. These are expressed in equation 3.11a and 3.11b. The other edge of the linear axis is left hanging free. This point cannot support a force, since there is no suspension of sorts and the moment acting on this section is therefore also 0 as expressed in equation 3.11d and 3.11c.

$$X(0) = 0 \qquad C = -D \tag{3.11a}$$

$$\frac{\partial X(0)}{\partial y} = 0 \qquad A = -B \tag{3.11b}$$

$$\frac{\partial^2 X(L)}{\partial y^2} = 0 \qquad C = -A\frac{\sin\beta L + \sinh\beta L}{\cos\beta L + \cosh\beta L} \tag{3.11c}$$

$$\frac{\partial^3 X(L)}{\partial y^3} = 0 \qquad \cos\beta L \cosh\beta L = -1 \tag{3.11d}$$

Values for βL which satisfy equation 3.11d correspond to the natural frequencies or resonance frequencies using the relation in 3.9c. This equation is called the characteristic equation. There are infinitely many solutions $\beta_n L$, but only the first three are regarded and these are calculated using a numerical solver. The characteristic equations and the first three solutions are shown in figure 3.6.

These solutions can then be used to visualize the deformation shapes of the first three resonance frequencies. The equation for the deformation shape is shown in equation 3.12 which is acquired from combining equations 3.11a through 3.11d with equation 3.10. The values β_n are the solutions to the characteristic equation. The corresponding frequencies are then calculated using 3.13. In figure 3.7 the first three deformation shapes and accompanying frequencies are shown.

$$X(y) = A\left[\sin\frac{\beta_n L}{L}y - \sinh\frac{\beta_n L}{L}y - \frac{\sin\beta_n L + \sinh\beta_n L}{\cos\beta_n L + \cosh\beta_n L}\left(\cos\frac{\beta_n L}{L}y - \cosh\frac{\beta_n L}{L}y\right)\right] \tag{3.12}$$

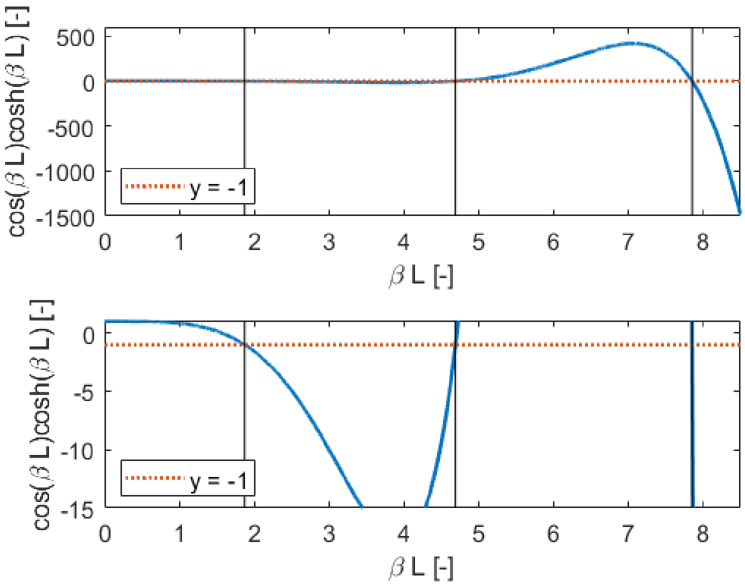

Figure 3.6: First three solutions for the characteristic equation 3.11d.

$$\omega = (\beta_n)^2\sqrt{\frac{EI}{\rho A}} = (\beta_n L)^2\sqrt{\frac{EI}{\rho A L^4}} \tag{3.13}$$

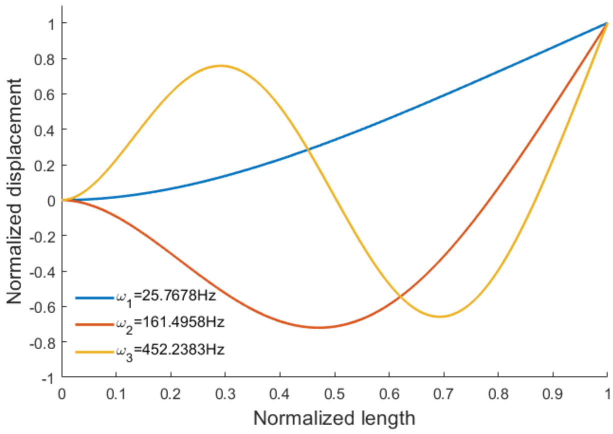

Figure 3.7: Mode shapes for the first three resonance frequencies.

Similar to the deflection study, a modal analysis is done for the cross section of the Y-axis. The results are shown in figure 3.8 which shows the first and fifth resonance frequency and accompanying mode shape which is exaggerated in order to clearly see the shape. Since it is a free vibration analysis there is no force applied and just the deformation mode shapes are shown. This is why the legend is a dimensionless scale ranging from 0 for no deformation and 1 for the maximum deformation. This mode shape is a deformation shape of the object at a certain frequency. The found shapes correspond well with the first and second mode shape found using the beam eigenfrequency analysis in figure 3.7. For the simulation, the second, third and fourth mode shapes showed bending of the beam in the z-direction, buckling of the thinner plate and a rotational mode.

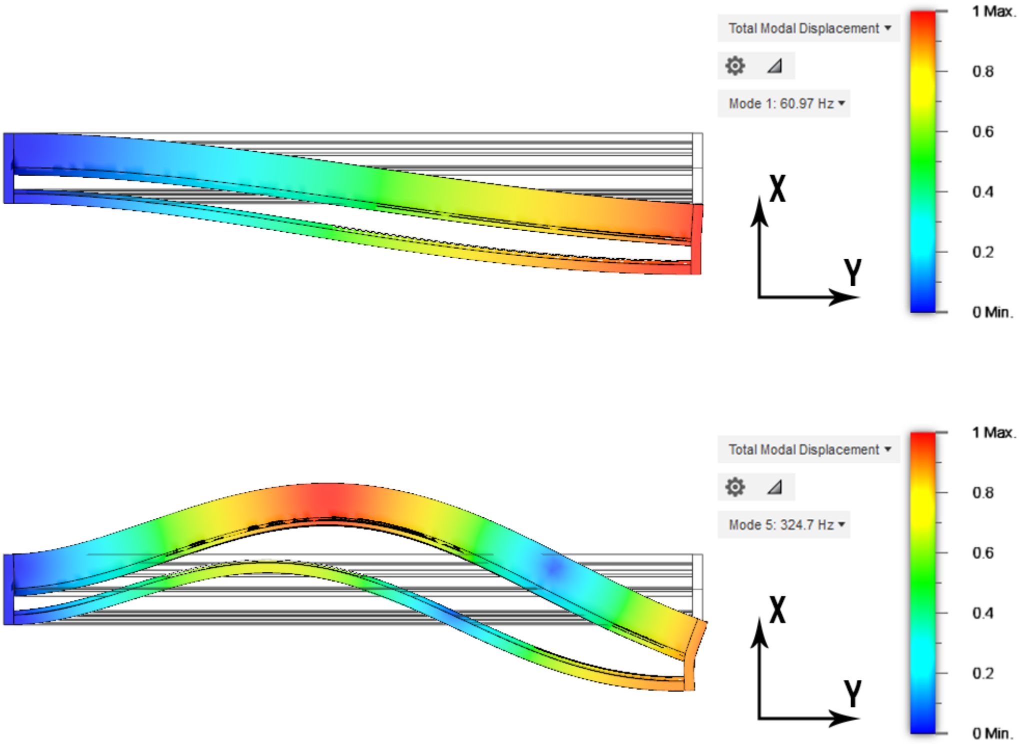

Figure 3.8: Simulated mode shapes of the Akribis linear axis. The legend is a dimensionless exaggeration in order to visualize the deformation.

The deflection due to the acceleration and deceleration of the X carriage will be comparable to the deflection of the beam due to gravity since the acceleration as mentioned in section 3.1 is comparable. As long as the changes in direction won't be in the same range as the first eigenfrequency, the deformation will be minor. The found eigenfrequency using the beam eigenfrequency analysis and the simulation are different due to the different cross section which is used and this is mostly done to get a feel for the order of the first eigenfrequency. The first eigenfrequency of the mounted Akribis axis will be different. The location of the Y carriage influences this. Having an additional mass near the free hanging end, will lower the frequency. But the carriage also adds to the bending stiffness of the axis, since the carriage is mounted with a wide base which will in turn increase the first resonance frequency. In practice the first eigenfrequency of the range 20-100 Hz will not be triggered when printing simple geometric shapes. Even when following the edge of the smallest possible circle at 500 mm/s with an acceleration of 10 m/s^2, the printer will only be able to perform 3.3 rounds in a second which is not in the same range as the first eigenfrequency. When the excitation frequency is at least five times smaller than the eigenfrequency, a static analysis of the deformation is sufficient since load and structural response will be acting in-phase and [16]. At lower velocities, the print head will be able to make a corner in a smaller amount of time and can move back and forth faster. Still it is unlikely that resonance will become an issue unless the print head is purposely moved back and forth over small distances at the highest acceleration possible. This could be done with the test set-up in order to test the frequency response of the system but this will only be done if deemed necessary and the set-up's results are not satisfactory. Still the first eigenfrequency is of interest and the higher resonance frequencies won't pose a risk towards the accuracy of the print head but give some insight in the way of deformation of the linear axis. The same discussion as with the deflection calculation of the material used and the exact mass of the components holds for this vibration analysis. The worst-case of using aluminium and using the high mass values is considered to be unrealistic. The acquired values therefore only give an indication of the deflection and vibrational frequencies and the system is deemed to be sufficiently stiff. Still it is advisory to use tool paths and related accelerations which do not overly stimulate vibration and resonance. A poor tool path would be fast movements from side to side over a small range of motion at high velocity.

3.3 Nozzle production

In order to research the bubble forming process, coaxial nozzles have to be designed and accurately produced. A three dimensional model needs to be made with parameters which can be tuned in order to better control the bubble forming process. The produced nozzles also need to be evaluated.

3.3.1 Nozzle design

The exact model used by Lewis' lab is not available but some images of the section view of a nozzle were available. These images were used as a baseline for the coaxial nozzle. This evolution of the nozzle model can be seen in figure 3.9.
The models are created with SOLIDWORKS. The actual nozzles are produced with a Formlabs Form 2 SLA 3D printer which is available at the University of Twente. This process is also based on using photopolymers as the primary material. A UV laser is scanned using galvano mirrors along a contour of a series of computer generated slices. This locally solidifies each layer of resin and it bonds to the previously polymerized layer. This process can achieve a very high accuracy and surface finish and is therefore commonly used for jewelry, dental applications and prototyping [17]. The 3D models need to be loaded in the slicer software which translates the 3D geometry into layers and writes this into machine code. A preview window of a set of nozzles with supports and base layer is shown in figure 3.10a. A finished batch of nozzles still attached to the printer build plate is shown in figure 3.10b.

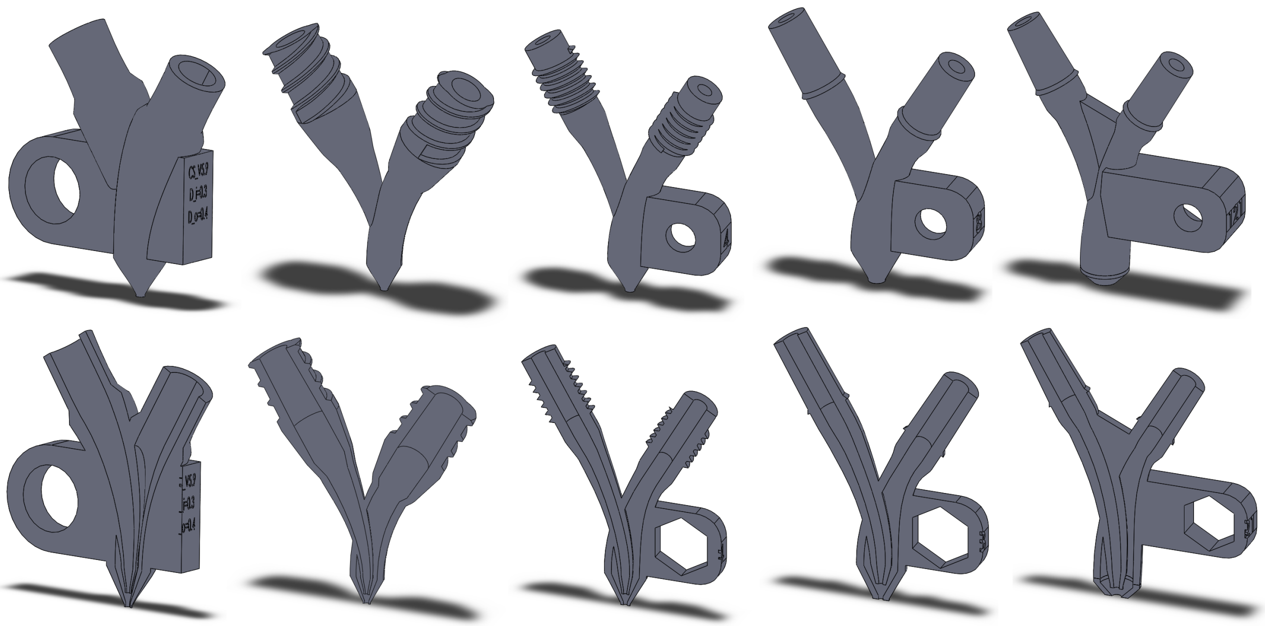

Figure 3.9: Iteration on nozzle and connector design.

In order to get to a working nozzle model which allows for producing bubbles through liquid and gas injection, several iterations of nozzles were manufactured. This was done to get a measure of the accuracy and consistency of the Form 2 and to get a baseline for a functioning nozzle. Each batch of nozzles had to be removed from the print bed and some post-processing was necessary. In order to print overhangs, the slicing software incorporates supporting structures as can be seen in figure 3.10a. These supports are not part of the model and have to be removed using a flush cutter. Uncured resin also remains in the printed model and on the surface of the printed model. This has

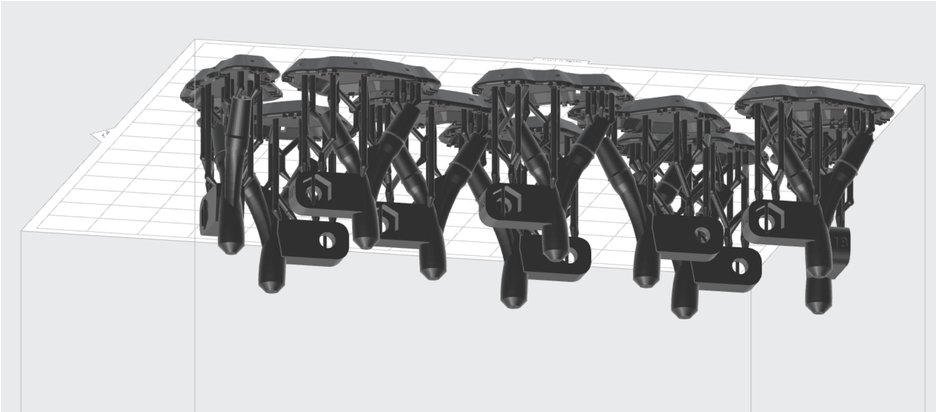

(a)

(b)

Figure 3.10: Figures showing a) the preview window of the slicer software and b) the Formlabs Form 2 SLA printer with a close-up of the finished nozzles ready for post-processing.

to be removed to prevent it from curing over time under influence of UV radiation. Models produced with sterolithography (SLA) are usually rinsed off of liquid resin in an isopropyl alcohol(IPA) bath. The inner channels also contain liquid resin and this material will clog the nozzles if not removed. For this purpose two syringes are filled with IPA and water, respectively. First the syringe filled with IPA is connected to the outer channel and flushed until only IPA is ejecting from the nozzle. Especially the used black resin is visibly different from the IPA. The process is repeated for the inner channel. Both channels are flushed twice to ensure no residual resin to be left behind. This process is then repeated for the syringes filled with water which makes sure that there is no IPA left in the channels which can be aggressive to cured resin over longer periods of time. A a final cleaning step syringes are filled with air and the channels are cleared from water in order for them to dry faster.

3.3.2 Fabricating nozzles that fit existing tubing connectors

The first batch of coaxial nozzles was printed with the purpose of scaling the connections and it was printed in clear resin. A Luer push fitting and a 1/16” threaded connection were modelled with changing parameters. For the model of the push fitting, the outer diameter was varied between 4.07 and

4.15 mm. The angle was varied between 1 and 1.6^o. For the threaded connection the outer diameter and the height of the threads were changed. The inner nozzle inner diameter was modelled to be 0.35 mm and the outer nozzle inner diameter was modelled as 0.4 mm which is similar to a model from Lewis' lab.

The resulting push fit models were in the right range and the connector with an inclining angle of 1^o and outer diameter of 4.15 mm was used for the following models. The threaded connectors were tried but it was found that the inner threads of the female 1/16" connector crushed the protruding threads of the 3d printed model. Products manufactured with SLA tend to show low toughness and a high level of brittleness due to the high cross-link density and inhomogeneous architecture [18]. The threaded connections were therefore discarded as a way of efficiently and repeatedly connecting the nozzle to the input flows.

3.3.3 Fabricating nozzles with reproducible nozzle diameters

The orifices from the coaxial nozzles from the aforementioned experiments were inspected and it was noticed immediately that the inner and outer nozzle orifices were both cured completely shut. There was no hole where the outer nozzle orifice should be and since clear resin was used, it was visible that there were no air pockets inside the nozzle and thus only cured and uncured resin as can be seen in figure 3.11a. The orifices were obviously too small for the machine. During the UV radiation exposure of the modelled areas, some neighbouring region is also exposed to a lower level of radiation due to diffraction of the unabsorbed UV radiation. This is mostly problematic in small circles where the encircled area is exposed from all sides and unwanted curing occurs. The orifices therefore need to be increased in diameter. Also for the following batches, black resin has been used which absorbs more of the UV radiation and therefore fewer neighbouring material is cured and more accurate features can be obtained [19].

The second batch with dimensions as in table 3.2 in black resin allowed for purging of the inner channel which meant that the inner channel, the inner nozzle and the outer nozzle were all not clogged during production. The outer channel was not able to be purged. When the syringe plunger was pulled back and then let go, it returned to its initial position. This meant that a partial vacuum was formed and the channel was clogged. From the design model section view it was found that the distance between the inner nozzle wall and the outer wall was too small for the SLA machine as mentioned by the design rules of the manufacturer [20] but these design rules are no exact science since these vary per manufacturer [21], [22]. The distance between inner nozzle and outer nozzle wall was monitored for all successive nozzles.
In the third batch the nozzle diameters for inner and outer nozzle were iterated between 0.45-0.6 mm and 0.6-0.8 mm, respectively. The distance between between the inner nozzle and the wall was iterated between 0.4-0.64 mm while iterating the angle of the wall and the height difference between inner and outer nozzle. The resulting nozzles were inspected and whereas with the previous batch most outer channels were clogged, for this batch six out of eight inner channels were clogged. The wall of the inner nozzle was modelled as 0.3 mm and according to the previously mentioned design rules, supported walls should be at least 0.4 mm thick or else they may warp. This may have caused the inner nozzle wall to be unstable and collapse. In the second iteration, the small distance between the inner nozzle and the outer wall caused the unstable inner wall to fuse to the outer wall while not clogging the inner channel. To prevent this from happening the inner wall has been increased in thickness to 0.4 mm. Batch 4 used a thicker inner nozzle wall. The larger five out of eight inner

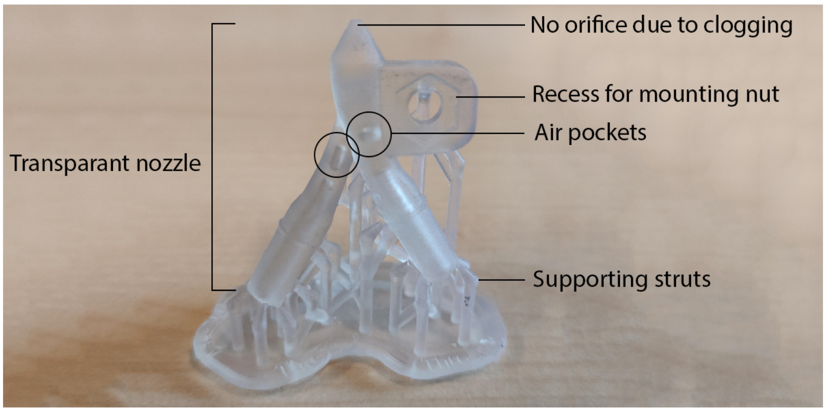

(a)

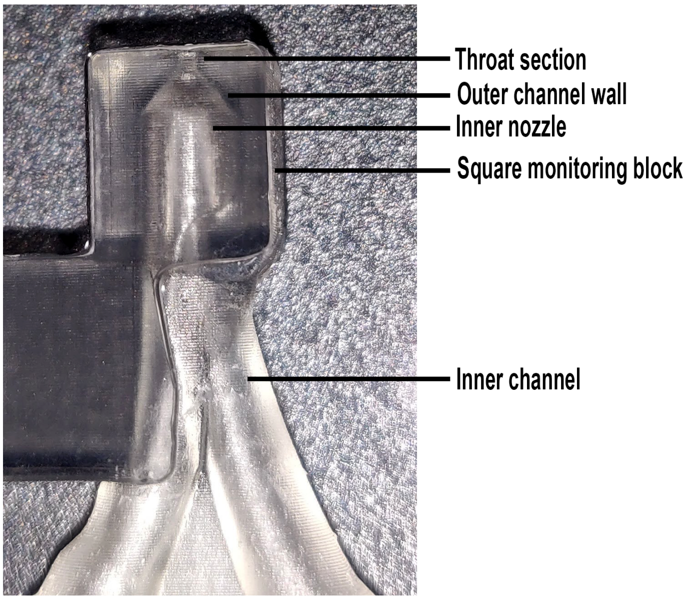

(b)

Figure 3.11: Close-ups of transparent nozzles a) showing a clogged nozzle in which some air pockets can be observed and b) showing a functional nozzle in which the air-filled channels can be distinguished from the cured resin.

nozzles were able to be purged. The outer nozzles were all purged from uncured resin. A transparent model of a coaxial nozzle where both channels were not clogged is shown in figure 3.11b. This figure shows the inner and outer channel geometry.

Accuracy and repeatablity of nozzle production

In the previous section it has been seen that the modelled geometry and the resulting 3d printed part are not the same. Small orifices and channels tend to clog during the printing process. This was also observed by S. Coco which caused inconsistencies in the resulting ejection phase [12]. This difference in actual diameter comes from the nature of the SLA printing process and the settings for the Formlabs printer. In order to have a stable process the intensity of the laser beam which scans the resin surface is higher than the intensity required for polymerization. The intensity profile of the laser spot looks like a Gaussian distribution meaning that resin is also irradiated outside of the spot diameter and also causes unwanted curing. The laser beam is traced along the resin surface and the resin is polymerized slightly outside of the laser track as can be seen in figure 3.12. With a lower intensity finer features could be accomplished but this could also result in mechanically weak prints, cloudy resin with flocks of cured resin and ultimately failed prints.

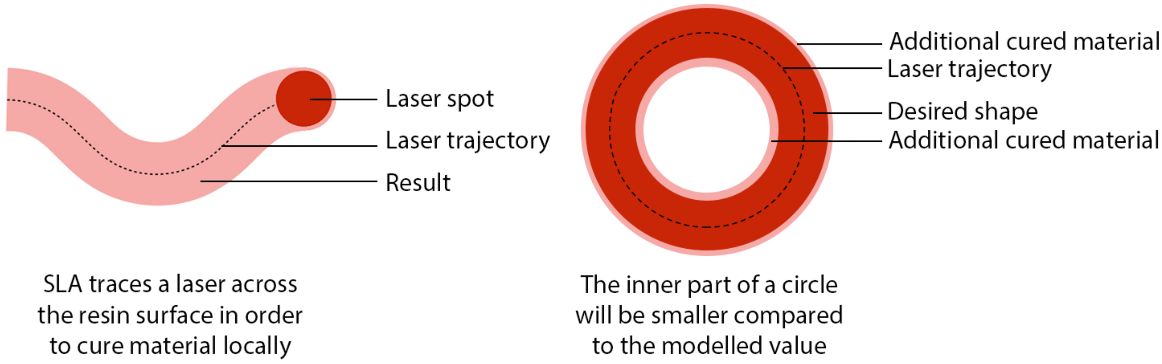

Figure 3.12: Schematic view of laser track and polymerized region in SLA printing.

In order to inspect how the printing process affects the printed nozzles, several sets of nozzle have been 3d printed. These sets are stated below:

- Iteration of outer nozzle diameter from 0.1 mm to 2.4 mm
- 25 nozzles in 3 batches with an outer nozzle diameter of 0.8 mm
- 11 nozzles with an outer nozzle diameter of 0.5 mm

The first set is to find the general trend and offset of the process and to see whether this offset from the modelled diameter becomes more regular for larger, less critical orifices. The second set shows the average measured nozzle size and the amount of variation between a set of nozzles with a similar modelled outer diameter and the variation between different batches from the 3d printer. The third set shows the average and the variance for a smaller and thus more critically modelled nozzle size. These nozzles were then inspected under a VHX-5000 digital stereo microscope where the diameter was measured and the overall surface quality was observed. In figure 3.13 three outer nozzles are shown with the measured diameter. This was done for all nozzles in the first set. These found values were then put up against the modelled value as shown in figure 3.14. This shows a clear trend in the results. Too small modelled outer nozzle diameters up to 0.3 mm do not show an orifice. The material in this hole was also exposed to some UV light and was therefore also polymerized. The nozzles which were modelled to be larger than 0.8 mm show a consistent offset of 0.2 mm. For the nozzles from 0.4 to 0.8 mm, the actual nozzle size converges to the 0.2 mm offset line. This can be explained with the previously shown figure 3.12. In a circular shape the inner region is has higher UV irradiance compared to the outer region. This effect is stronger for smaller orifices.

In order to check the repeatability of the nozzle production process, the second and first set of nozzles were examined. The results are shown in figure 3.14 as the errorbars. Both sets of nozzles do correspond with the previously found offset line. The average of the larger modelled holes at 0.8 mm was closer to the 0.2 mm offset line than the nozzles modelled to be 0.5 mm. This also corresponds with the previously found phenomenon where smaller holes tend to clog and thus become smaller. As can be seen in figure 3.13, the smaller nozzles also showed some inconsistency in its circular shape. The standard deviation of both nozzle sizes was similar at around 30 microns which is acceptable. In order to accurately compare nozzle performance in the following experiments,

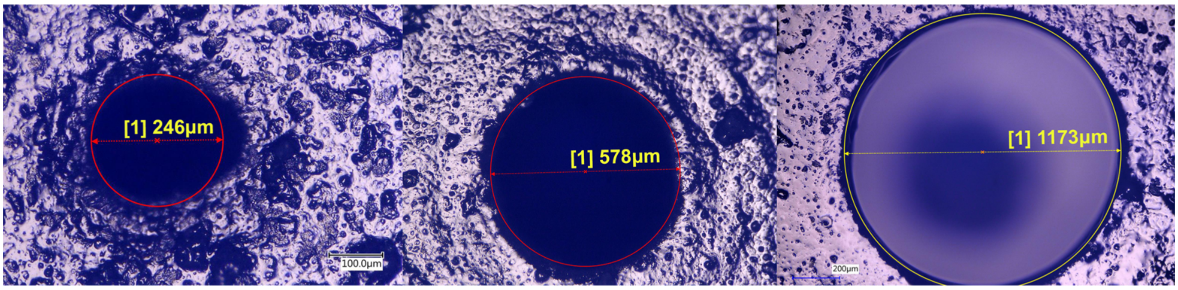

Figure 3.13: Nozzles modelled at 0.5 mm, 0.8 mm and 1.4 mm, respectively.

the outer nozzle diameter for all used nozzles has been checked under the microscope and this diameter is used in calculations.

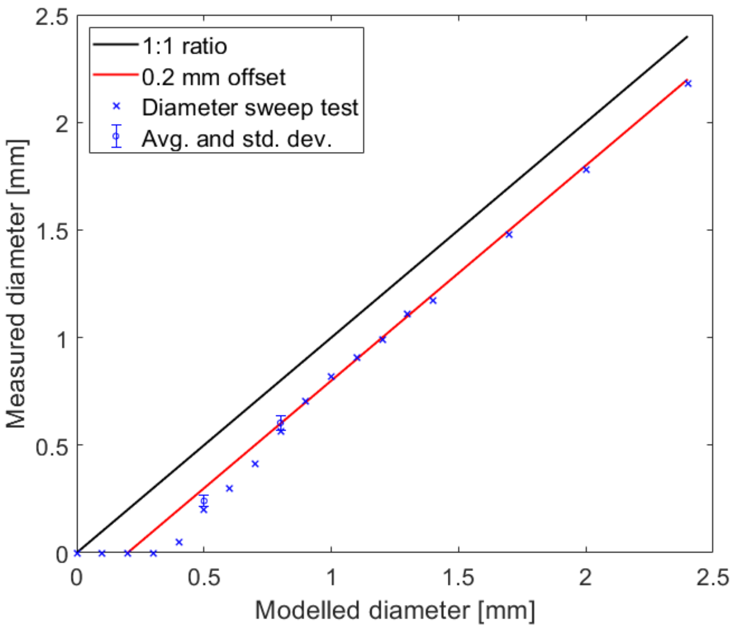

Figure 3.14: Measured diameter as a function of the modelled diameter and the measured variance for for outer nozzle orifices modelled at 0.5 mm and 0.8 mm.

Resulting outer nozzle for nozzles without throat section

Also a batch of nozzles was produced without the throat section as can be seen in figure 3.15. These nozzles were produced and inspected under the microscope. The variance of the outer nozzle diameter for these nozzles was similar to the previously found values in figure 3.14 but the measured diameter was now close to the modelled diameter. As can be seen in figure 3.10b, the 3D printing process finishes with the outer nozzle. This outer nozzle section is an overhang, meaning that the next layer is extending beyond the previous layer without direct support. The steepest outer nozzle wall angle in the wall angle iteration is 25^o. The result is shown in figure 3.16a. The steep overhang causes the curing material to not properly adhere to the previous layer and some recesses and deviation from the modelled circle are the result. The rest of the nozzles without throat showed outer nozzles smooth outer nozzles without much deviation from the modelled circle and one nozzle is shown in figure 3.16b.

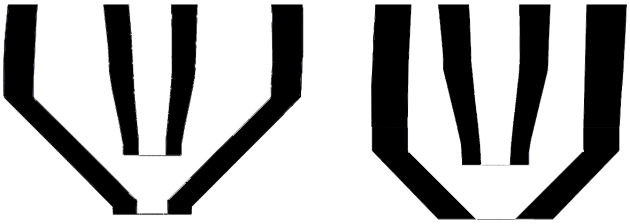

Figure 3.15: Section view of nozzles with (left) and without throat section (right)

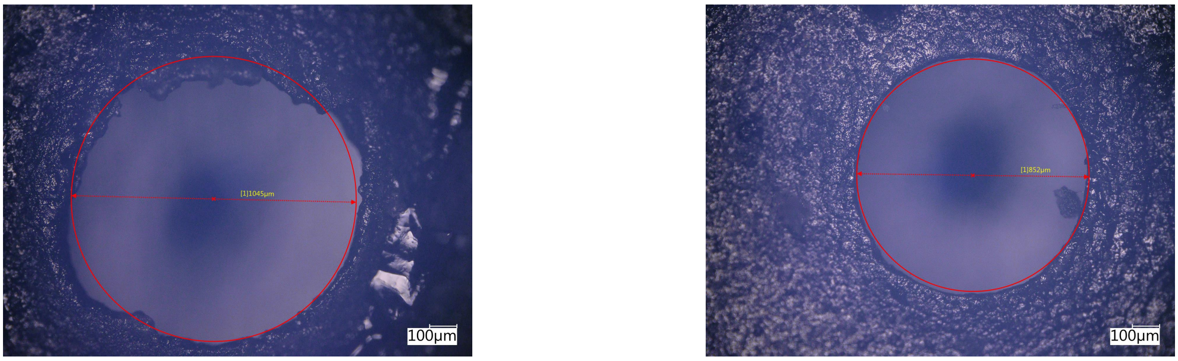

(a) (b)

Figure 3.16: Microscope image of two nozzles without throat with control parameters a) D_o=0.8 mm, Θ=25^o, H=0.93 mm. b) D_o=0.8 mm, Θ=35^o, H=0.93 mm.

Confirming design rules

A batch of nozzles was made with dimensions as in table 3.2. All of the nozzles were able to be purged which meant that both the inner as outer channels were not closed off during printing. These past batches have resulted in a series of design rules which are used in further modelling of nozzle geometries. These design rules are as follows:

1. Inner nozzle diameter D_i should be 0.6 mm or higher
2. Outer nozzle diameter D_o should be 0.6 mm or higher
3. The distance between inner nozzle and outer nozzle wall should be larger than 0.4 mm
4. The SLA printer should use 0.1 mm layer height increments

Table 3.2: Nozzle dimensions for subsequent batches, numbers in parentheses were unknown at the time or not modelled consciously.

Batch no.	D_i [mm]	D_o [mm]	θ [°]	Distance inner nozzle to wall [mm]	Notes
1	0.35	0.4	(60)	(0.19)	Fully clogged
2	0.4-0.55	0.45-0.6	(60)	(0.3)	Clogged outer nozzle
3	0.45-0.6	0.6-0.8	45-60	0.4-0.65	Clogged inner nozzle
4	0.45-0.6	0.6-0.8	40-55	0.42-0.49	Partial success
5	0.6	0.8	40-60	0.48-0.51	Success

5. The nozzle walls should be at least 0.4 mm thick
6. Black resin is used for more accurate features
7. The height difference between the inner and outer nozzle H and the angle of the outer nozzle wall θ can be changed in order to increase/decrease the distance between the inner nozzle and the outer nozzle wall

3.4 Experimental set-up

In order to control the liquid and gas supply and to be able to record the results a set-up is required. A schematic drawing of the required set-up is shown in figure 3.17a. This shows a syringe pump supplying the liquid flow, a pressure controller sustaining the gas pressure with an incoming air flow. These flows come together in the coaxial nozzle which is further discussed in section 4.1.

3.4.1 Controlled liquid supply

The liquid supply is done using the N-4000 Two channel syringe pump which ensures a continuous steady flow. This syringe pump allows the placement of two syringes which allows for a larger volume to be used which allows for a longer range of time in which experiments can be done. For two syringes of 50 mL the maximum flow rate is 121 mL/min per syringe. The liquid used in these experiments is water with the surfactant Tween 80. A surfactant reduces the surface tension between the liquid and gas interface. This way the formed bubbles are more stable [23]. The critical micelle concentration is the concentration at which the surfactant molecules start to cluster apart from being at the interfacial regions. This concentration is 13-15 mg/L but it has been shown that the surface tension still decreases which is why 0.4 wt% has been used in the experiments [24]. The resulting surface tension for the liquid is around 39 mN/m and this value is used in further calculations [24]–[26].

3.4.2 Controlled gas supply

The gas pressure is controlled with a pressure controller. Gas is compressible and to get a flow through the nozzle first a pressure differential has to be developed. If a flow controller is used, some of the gas is used to build up the pressure in order to get flow through the nozzle. By using a pressure controller, the pressure in the inner channel is set and a steady state is reached and gas flows steadily through the nozzle. A consistent volume flow is achieved. The pressure controller is supplied by Bronkhorst and is calibrated in the range from 0.6 to 30 kPa(g). The device is rated to be 0.5 % accurate at full scale so $\pm$ 0.15 kPa(g). At first this device is controlled over an RS232 connection but it does support the EtherCAT protocol over which the motion controller communicates with the servo drives so the pressure controller can be connected to this network and driven from the motion controller. For the experiments the appliance has been used through supplied software which allowed for the implementation of scripts. This allowed for the automation of the experiments. Compressed air is used as the introduced gas.

3.4.3 Visualizing bubble ejection

The ejecting liquid is moving rapidly, which requires a fast shutter speed in order to prevent motion blur. The used camera is an IDS 1240ML with a shutter time as little as 9 microseconds. This shutter time is sufficient as verified with the rule of thumb of Versluis which incorporates particle size and its velocity [27]. These can be obtained from previous research as shown in figure 2.5a and 2.5b and a shutter speed of 33 microseconds is calculated to be sufficient. The light which enters the sensor in this time period is small and therefore a substantial light source is used as can be seen in figure 3.17b. Diffuse light gives a more even background for the images and therefore several layers of translucent plastic have been mounted in front of the LED array. The camera is mounted in the set-up using Blocan optical posts as can be seen in figure 3.17b.

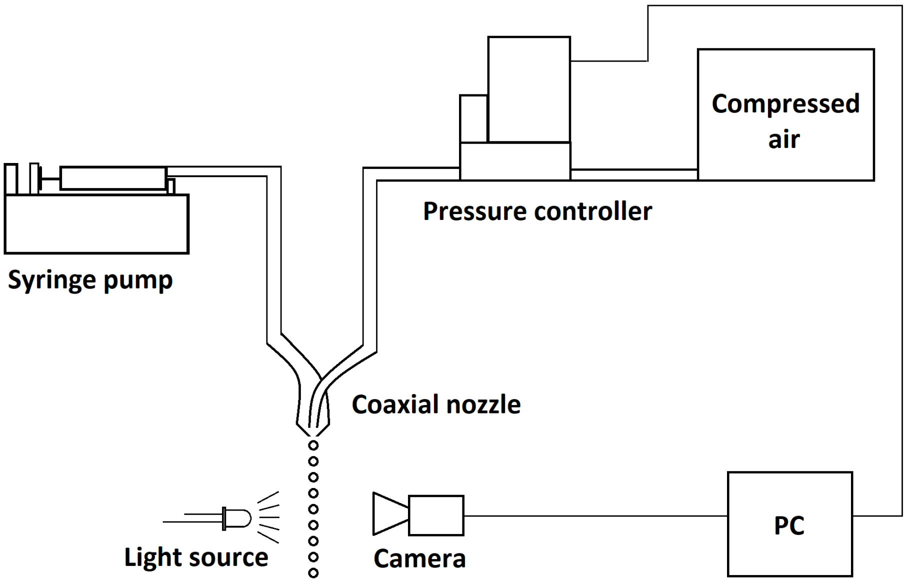

(a)

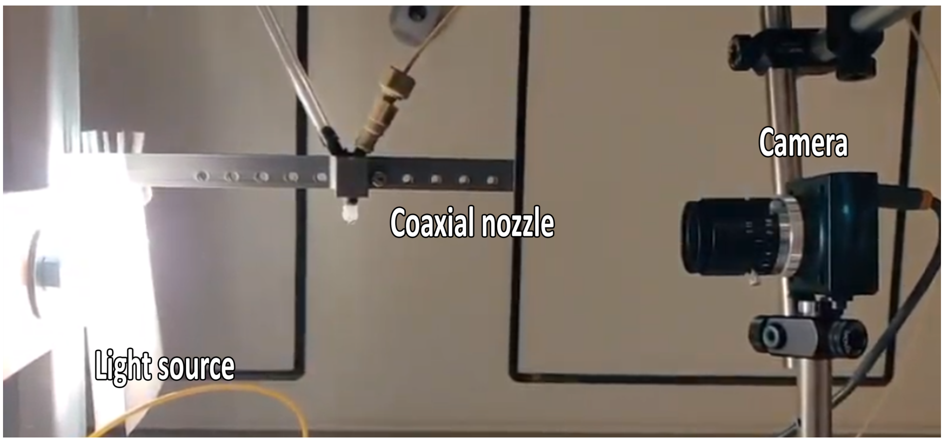

(b)

Figure 3.17: Figures of the set-up for the ejection identification with a) a schematic drawing of the set-up. b) Photograph of part of the set-up where the liquid and gas flow enter the nozzle and the resulting phase is captured using a camera.

3.4.4 Procedure of performing experiments

The syringe pump is controlled manually. A liquid flow rate is set on this device. The pressure controller is operating according to a script which is run from a PC. After each iteration of pressures, the liquid flow rate is changed. The camera is run from the same PC as the pressure controller and was synchronized to take 10 photographs of each experiment at a specific pressure and liquid flow rate. There is some time delay between the pressure change and the photographs in order to bridge the settle time of the controller. After each set of experiments with a single nozzle, this nozzle will have to be manually removed and replaced with a successive nozzle. The syringes will have to be refilled at each nozzle change in order to have sufficient liquid supply for a set of experiments.

3.4.5 Conclusion on setup design

The set-up allows for the precise control over liquid flow and supplied gas pressure. The resulting ejection can be captured using the high shutter speed camera. The images for each experiment can then be evaluated in order to determine the ejection phase. The limitations for this set-up are the pressure range of the pressure controller and the maximum force of the syringe pump. As a low viscosity liquid is used, the maximum force of the syringe pump is sufficient. The pressure in the nozzle is highly dependent on the nozzle dimensions and supplied liquid flow and it will be apparent that the pressure range is suitable for most experiments, but not all.

Chapter 4

Study of bubble ejection dynamics

In order to inspect the effect of changing nozzle geometries, several parameters which define a nozzle geometry have been defined. A base nozzle has been designed with the previous design rules as found in section 3.3.3. The change in ejection phase will observed while changing each control parameter individually. This way the effect of each parameter can be found.

4.1 Geometric control parameter iterations of the nozzle to scan the control parameters for bubble formation

A schematic view of a section of the nozzle is shown in figure 4.1. The parameters which will be changed are the inner nozzle diameter D_i, outer nozzle diameter D_o, the height H between the inner and outer nozzle, and the outer wall angle Θ. These changing parameters and corresponding nozzles are shown in table 4.1. The values in the table correspond to the parameters in figure 4.1.

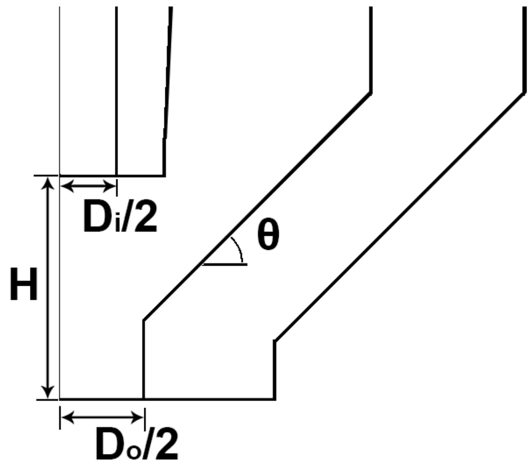

Figure 4.1: Schematic section of the nozzle and important parameters.

The previously designed nozzles have been produced and can be mounted in the set-up. Some nozzle geometries were in conflict with the found design rules mentioned in appendix 3.3.3. With a distance between the inner and outer nozzle of 1 mm, the distance between the inner nozzle and the outer nozzle wall was measured in the model as 0.21 mm and the nozzle clogged during production. The nozzle with an inner nozzle diameter of 1.5 mm had a modelled distance of 0.28 mm between inner nozzle and outer nozzle wall but this one was able to be cleaned. The nozzle with an outer

Table 4.1: Modelled nozzle geometries where each geometric parameter is iterated through.

Nozzle No.	D_i [mm]	D_o [mm]	H [mm]	Θ [^{o}]
40	0.7	0.8	1.5	45
41-45	0.6-1.5	0.8	1.5	45
46-51	0.7	0.6-2.4	1.5	45
52-56	0.7	0.8	1-4	45
57-61	0.7	0.8	1.5	20-60

wall angle of 60 ^{o} had a modelled distance between inner nozzle and outer wall of 0.27 mm and this nozzle was clogged after production. The nozzles with both channels accessible have been used for further experiments.

In order to find relevant liquid flow rates and gas pressure values which will give a large overview of the phases, some small experiments have been done. For several distinct nozzles the transitions from ejection phase without gas to a ejection with gas encapsulated in the liquid to an unstable spray ejection have been noted. An example for these transitions can be seen in figure 4.2. For smaller outer nozzle orifices the pressures for transition were higher compared to larger orifices. In order to get an overview of input pressure and liquid flow and the resulting phases for a large diversity of nozzle geometries, a broad input spectrum was selected. These following data points have been used as input for every one of the nozzles.

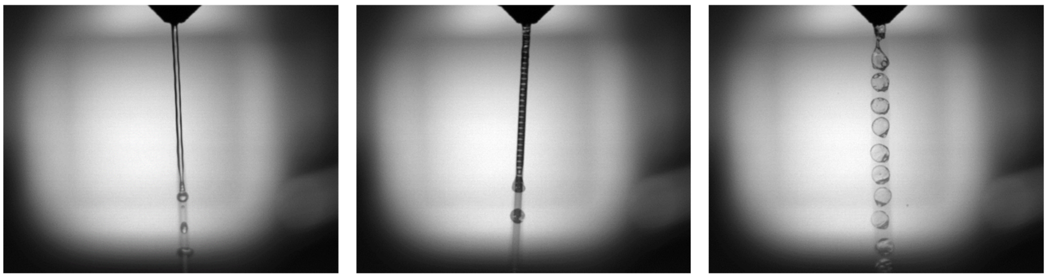

Figure 4.2: Photographs showing the phase at a constant liquid flow rate and increasing pressure.

$$\begin{aligned} P &= \begin{bmatrix} 1 & 2 & 3 & 4 & 6 & 8 & 12 \end{bmatrix} \text{ kPa} \\ Q &= \begin{bmatrix} 8 & 12 & 18 & 24 & 30 \end{bmatrix} \text{ mL/min} \end{aligned} \tag{4.1}$$

Each nozzle will be mounted in the set-up and for each of these experiments 10 photos will be taken for evaluation of the ejection phase which are elaborated upon below.

4.2 Results

4.2.1 Observed ejection phases

The experiments resulted in photographs which showed the ejection phase per data point. The occurring phases are classified as follows and the labels a through i correspond to the labels in figures 4.3 and 4.4 where each of the phases is visualized:

a Dripping, droplet growth on the nozzle until the gravitational forces become too large

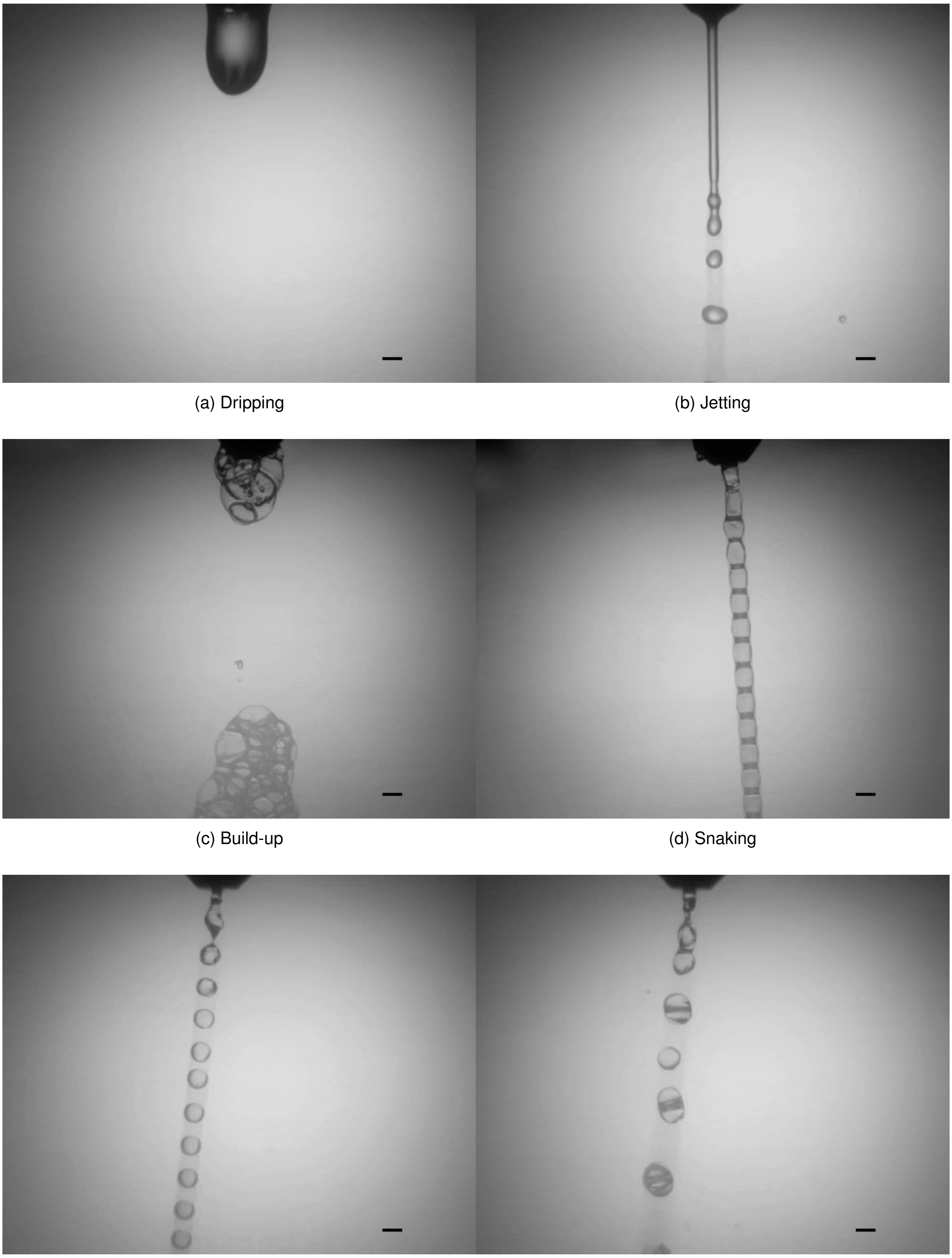

(a) Dripping

(b) Jetting

(c) Build-up

(d) Snaking

(e) Monodisperse bubbles

(f) Multidisperse bubbles

Figure 4.3: Photographs of each of the present phases which appear in the phase diagrams. Scale bars: 1 mm.

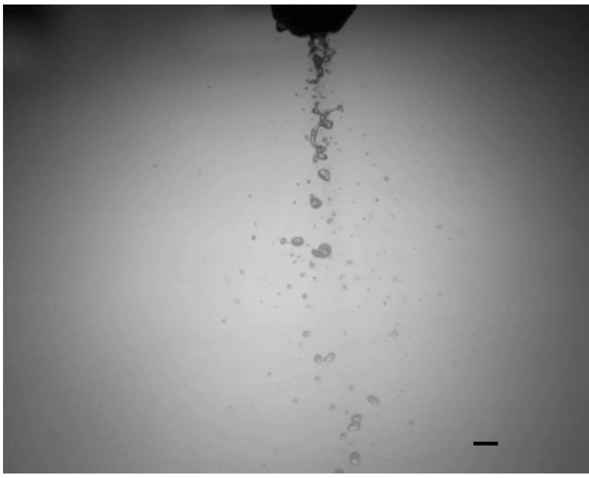

(g) Spraying

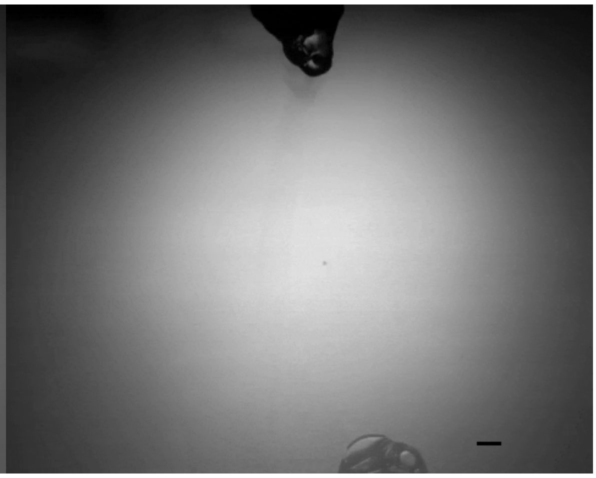

(h) Combination build-up and multidisperse

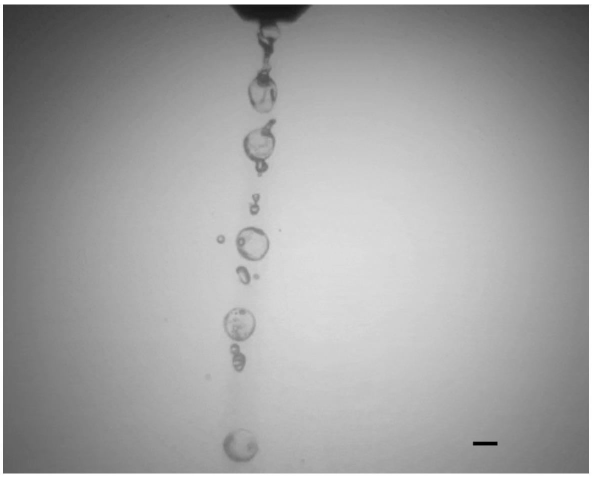

(i) Combination Spray and multidisperse

Figure 4.4: Photographs of each of the present phases which appear in the phase diagrams. Scale bars: 1 mm.

b Liquid jet, a continuous liquid column is ejected from the nozzle.

c Build-up of bubbles around the nozzle which grow in number of bubbles and then collectively eject from the nozzle.

d Snaking, where a continuous connected column of bubbles leaves the nozzle.

e Monodisperse bubbles, bubbles of a single diameter leave the nozzle.

f Multidisperse bubbles, more unstable form of bubbles which shows several diameters of bubbles.

g Spray, uncontrolled ejection of tiny droplets from the nozzle. There is no gas encapsulation.

h A combination of build-up and bubbles

i A combination of spray and bubbles

For each of the experiments the resulting ejection phase has been extracted and this can be used to get some understanding in the effects of changing the nozzle inner geometry on the ejection phase. The experiments for a single nozzle can be put in a single figure which maps the input gas pressure, the liquid flow rate and the resulting ejection phase. An example is shown in figure 4.5.

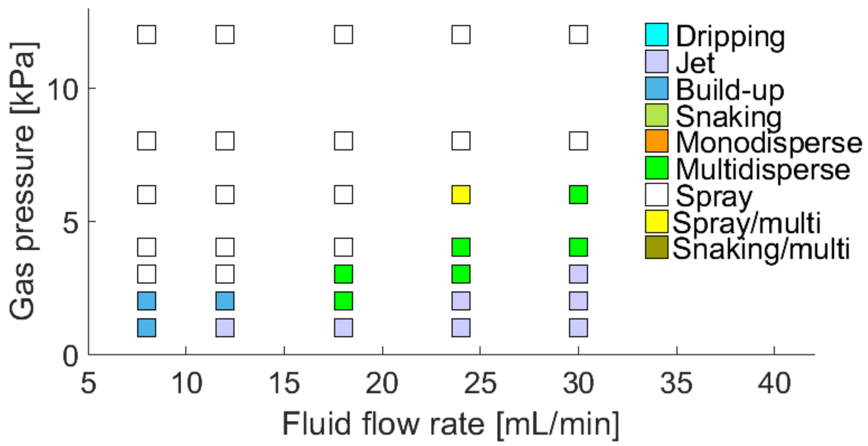

Figure 4.5: Phase diagram showing the nozzle ejection phase for varying liquid flow rate and gas pressure. Nozzle control parameters: D_i=0.6 mm, D_o=0.8 mm, H=1.5 mm, Θ=45^o.

The phase diagram shows the varying ejection phases for varying liquid flow rate and gas pressure. For low liquid flow rates and gas pressure the ejection shows as build-up. When increasing the gas pressure this transitions to spray. For higher liquid flow rates liquid jet is common which transitions into multidisperse bubbles which then transitions into spray. It can also be seen that the pressure at which the transitions from pure liquid in the ejection to gas introduction to spraying occurs, increase for increasing liquid flow rates. From a single phase diagram not much can be said and therefore multiple phase diagrams corresponding to a nozzle geometry parameter iteration have been put next to each other.

Phase diagrams for nozzle iterations with throat section with changing height, inner and outer nozzle diameter and outer nozzle wall angle

The resulting phase diagrams can be seen in figures A.2a through A.5a in appendix A.

These phase diagrams show mainly the build-up phase at lower pressures and liquid flow rate. At higher pressures mainly spray is observed. There are some exceptions which show very different behaviour. These are expected to be due to printing errors due to the model not conforming to the design rules in table 3.3.3. For increasing liquid flow rate phases like jetting appear which transitions to snaking, multidisperse bubbles and spraying. It is expected that phases like snaking and mono- and multidisperse bubbles can be used for the direct bubble writing process and the performance of a nozzle geometry is therefore coupled with the number of appearance of these phases. From the developments of each of the phase diagrams in these figures some things can be observed. These are listed below:

- The inner nozzle diameter does not have a large influence. From the phase diagram in figure A.2a it can be seen that all nozzles don't show usable phases for low liquid flow rate. The two nozzles with the smallest inner nozzle diameter seem to perform the best along with the last nozzle with the largest inner nozzle. The second to last nozzle in this series is shown in figure 4.6a and this shows relatively stable bubble formation. After further inspecting the phases, the last nozzle does not seem usable with inconsistent and small multidisperse bubbles and also non-steady snaking phases as can be seen in figure 4.6b and 4.6c. Note the deviation from a straight line in the snaking phase. This also causes the bottom part to not be in focus. The distance between inner nozzle and outer wall again might have some influence here.
- Too large distance between nozzles does not allow for results. In figure A.4a it can be seen that the last two nozzles which have the largest distance H mainly show jetting and spray. The other nozzles show phases like multidisperse bubbles and snaking which are deemed useful for the direct foam writing process.
- The outer wall angle does not have that large of an influence. In figure A.5a the nozzle set is shown which iterates the outer wall angle. The last nozzle has a outer wall angle of 50 ^{o} and this nozzle therefore has the smallest distance between the outer wall and inner nozzle. This has resulted in a poor performing nozzle which mainly shows dripping and spray. The other nozzles show some usable phases with not much notable difference in performance.
- The outer nozzle diameter has some influence. Figure A.3a shows the iteration for a decreasing outer nozzle diameter. Nozzle 47 shows very inconclusive results which should be left out. The larger nozzles mainly show snaking for lower liquid flow rates. For the largest flow rate at 30 mL/min there is some snaking and multidisperse phase showing. In order to better view the influence of the outer diameter an additional phase diagram is made.

In order to inspect nozzles with small deviations in the outer nozzle diameter, several nozzles with slightly decreasing nozzle sizes have been put into a single phase diagram. The modelled diameter for all these nozzles was set to be 0.8 mm, but since the SLA process results in some variance in the actual measured diameter as seen in figure 3.14 there are slight deviations from this value. The nozzles from table 3.2 have all been measured under the microscope. Nozzles with a measured outer nozzle diameter ranging from 0.6155 μm to 0.5340 μm were put into a single phase diagram which is shown in figure 4.7. The corresponding nozzle geometries are visualized in the figure and show the changing parameters like inner nozzle diameter and inner to outer nozzle height.

For the lower liquid flow rates mainly build-up is present, but for higher flow rates there is a clear distinction between a purely liquid jet, and a phase where gas is introduced like snaking or multidisperse bubbles. There also seems to be a strong correlation with the outer nozzle diameter as the transition pressure increases with decreasing nozzle size. This transition from purely liquid to gas introduction has been thoroughly investigated by S. Coco and C.W. Visser as mentioned in

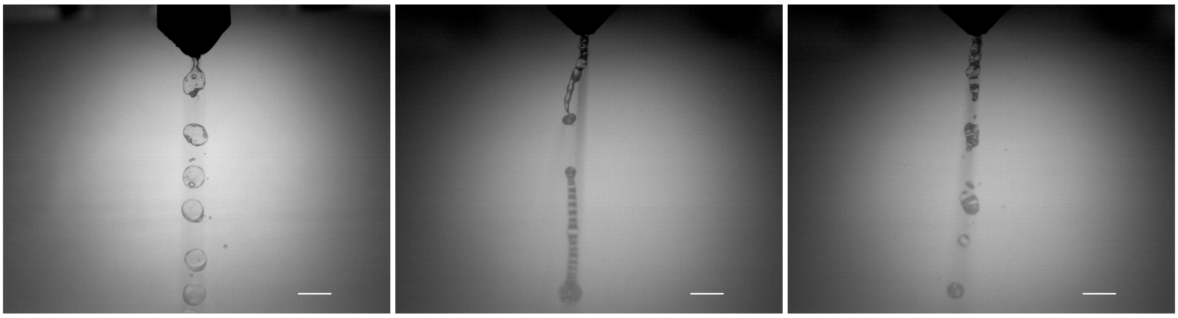

(a) (b) (c)

Figure 4.6: (a) Multidisperse bubbles nozzle 43 (D_i=1.1 mm, D_o=0.8 mm, H=1.5 mm and Θ=45^o) (b) Snaking nozzle 45 (D_i=1.5 mm, D_o=0.8 mm, H=1.5 mm and Θ=45^o) (c) multidisperse bubbles nozzle 45 (D_i=1.5 mm, D_o=0.8 mm, H=1.5 mm and Θ=45^o). Scale bars: 5 mm.

chapter 2. The modeled transition pressure in equation 2.1 consists of a dynamic pressure, capillary pressure and a friction pressure drop. This model can be used to calculate the transition pressure from purely liquid to gas introduction for each of the nozzles at a certain flow rate.

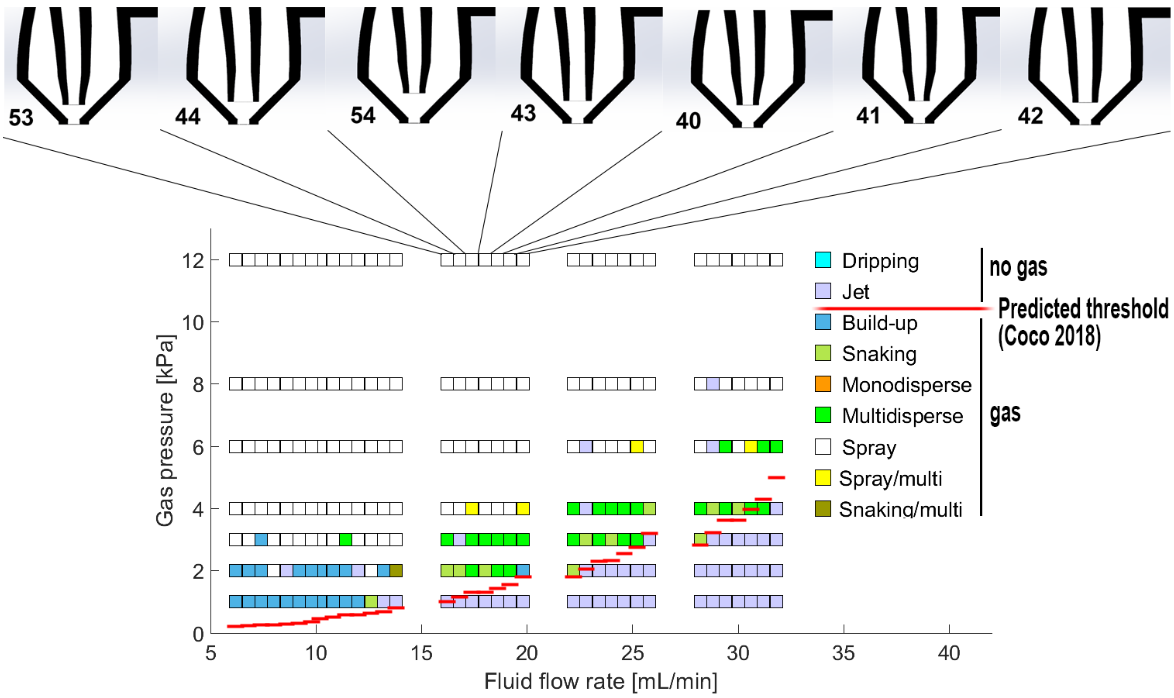

Figure 4.7: Phase diagram for nozzles with decreasing measured outer nozzle diameters. Nozzle control parameters: D_i=0.6-1.3 mm, D_o=0.8 mm, H=1.3-2 mm, Θ=45^o.

In the calculated transition pressure, the nozzle parameters D_i, D_o and H have been used to calculate the pressure components. This predicted transition pressure is shown in the figure as the red bars. At low liquid flow rates, the Bernouilli pressure and pressure loss due to friction components are low. The capillary pressure component is dominant but as can be seen in figure 4.7, the calculated transition pressure is lower than the controlled pressure data points. This explains why the phases at lower liquid flows already have gas introduction and show build-up and spray. At higher liquid flow rates, the liquid velocity is higher and with this the Bernouilli pressure and pressure loss due to friction increase. The calculated transition pressure is within range of the pressure data points and for lower pressures liquid jet is apparent and around the calculated transition pressure this transitions into snaking and other phases with bubbles. In order to validate the model further and to get further insight an attempt has been made to incorporate all experiment results in a single graph by using dimensionless parameters.

Dimensionless plot for nozzles with a throat section with changing height, inner and outer nozzle diameter and outer nozzle wall angle

The experiment pressure can be made dimensionless by using the ratio relative to the calculated transition pressure. If the pressure ratio value P/P$_{tot}$ is lower than 1 then no gas introduction is expected in the experiment phase. For a pressure ratio higher than 1 phases with gas introduction are expected such as build-up, bubbles and spray.
On the horizontal axis the Weber number is used which is a dimensionless number which relates inertial forces to interfacial forces and dictates which of these forces is dominant [28].

$$We = \frac{\rho_l R_o v_l^2}{\sigma} \tag{4.2}$$

In this equation ρ_l is the density of the liquid, R_o is the radius of the outer nozzle, σ is the surface tension for the used liquid and v_l is the liquid velocity calculated from $v_l = \frac{Q}{A_o}$. The Weber number is used as a measure to determine the transition between the dripping regime and jet formation. For lower Weber number the surface tension dominates and the incoming liquid adheres to itself and the surface tension forces keep it from detaching from the nozzle until the gravitational force becomes too large and the drop detaches. For higher Weber number the inertial forces are dominant and the liquid is ejected from the nozzle in a continuous liquid column.The transition from dripping to jetting is stated to be between 1 and 10 and frequently $We > 4$ is used as the transition value [28]. For the data points acquired from the experiments, the resulting pressure ratio and Weber number have been calculated and these were put onto a log scale. This resulted in figure 4.8.

In this figure a horizontal line has been drawn marking the pressure ratio being equal to one. Also the measurements of S. Coco have been drawn as error bars which naturally lie around the horizontal line. Below the horizontal line mainly the jetting phase is observed which confirms the gas introduction transition model from S. Coco [12]. The Weber number for these measurements is larger than 4 and therefore no dripping is observed. Above the horizontal line there are some regions to be distinguished. For lower Weber number there is a clear transition from build-up to spray. For higher Weber number there is a cluster of multidisperse bubbles and there appears to be some grouping of the snaking phase. In this figure four nozzles which showed inconsistent results were removed from the data set. These results included dripping and jetting phases at pressure ratios higher than 10. The nozzles these results belonged to were previously mentioned in section 4.2.1 as nozzles with either a small distance between inner nozzle and outer nozzle wall or nozzles with a large distance between inner and outer nozzle.

Some experiments have been excluded because of inconsistent results or because the related nozzle was clogged during production. With some knowledge of this first set of nozzles a second set of nozzles was designed.

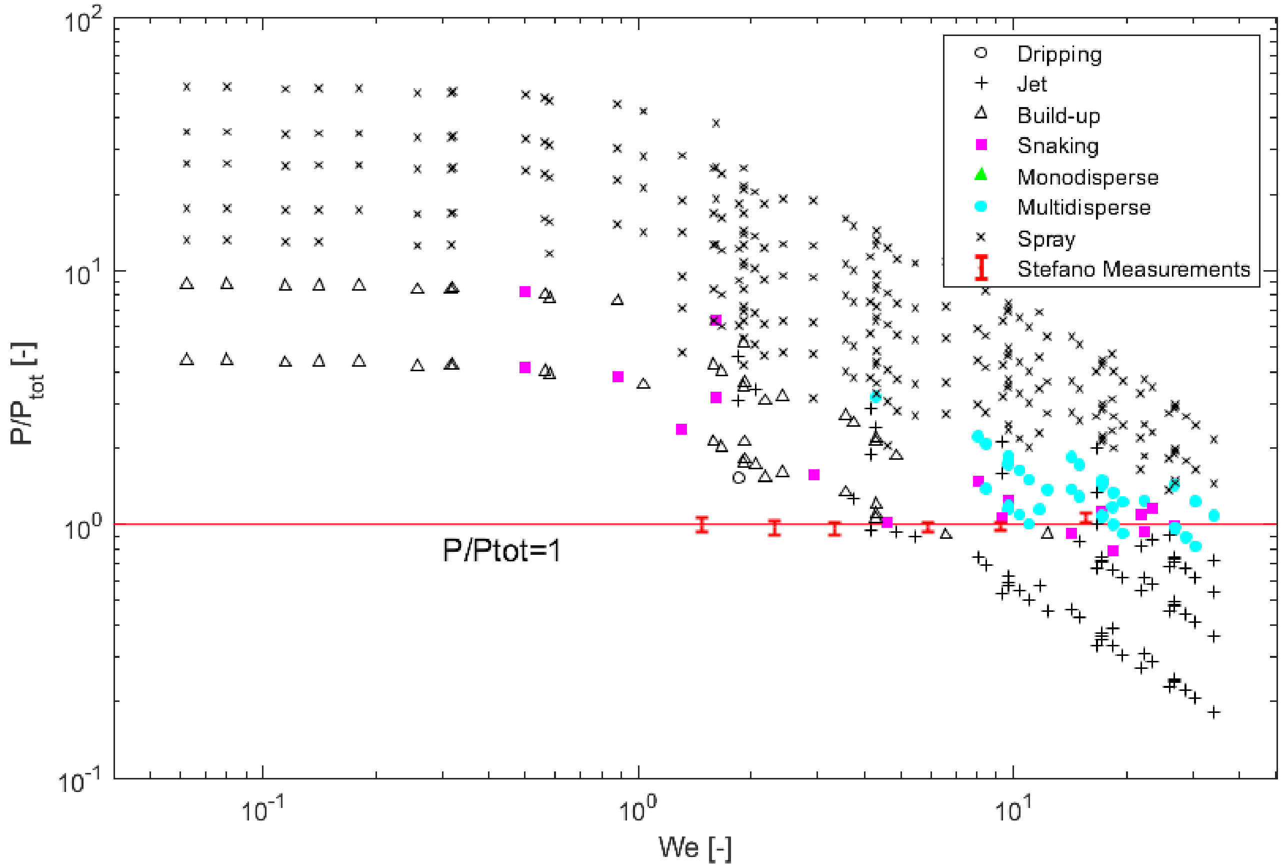

Figure 4.8: Dimensionless plot mapping the pressure ratio as a function of the Weber number and the resulting phase with some nozzles excluded.

4.2.2 Design iteration 1: Nozzles without a throat section and changing height, outer wall angle and outer diameter

From the first set of nozzles it was apparent that a too large distance H between inner and outer nozzle was not beneficial for the resulting process. In order to be able to decrease this distance the throat section of the outer nozzle was not included in the model. This change is visualized in figure 3.15 where the previous design and the new design iteration are shown next to each other. Also the diameter of the inner nozzle did not really influence the process unless the distance between inner nozzle and outer nozzle wall became too small. This inner diameter was therefore kept constant. The parameters which were iterated are shown in table 4.2. The last two iterations show the iteration of the outer nozzle diameter. One iteration with a constant height between inner and outer nozzle. The inner nozzle is moved up in the model to accomplish this constant height. The other iteration of the outer nozzle diameter shows a constant inner cross section where for each nozzle a slice of the outer nozzle is removed in the SOLIDWORKS model thus effectively increasing the outer diameter.

Phase diagrams for nozzles without a throat section and changing height, outer wall angle and outer diameter

The nozzles were mounted in the set-up and the resulting phases for the data points were again extracted. This resulted in the phase diagrams in figures figures A.6 through A.9 in appendix A. The phase diagram for increasing height between inner and outer nozzle is shown in figure A.6a. Again for lower liquid flow rates the input pressure is above the expected transition pressure and build-up and afterwards spray is observed. For higher flow rates again the transition from jetting to gas introduced phases visible and the pressure is similar for all nozzles. When looking at the results at 30 mL/min it appears that a larger distance between inner and outer nozzle produces a wider range of usable phases as can be seen in figure 4.9 where stable bubble formation was achieved between 2 and 4 kPa.

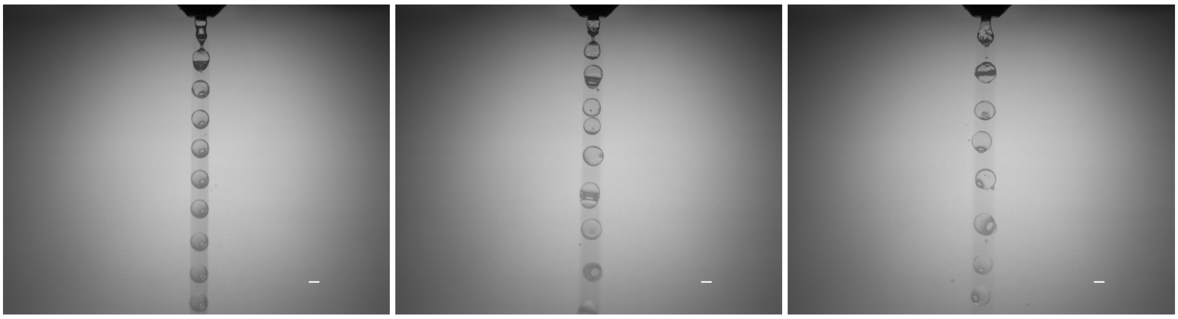

(a) (b) (c)

Figure 4.9: Resulting ejection phases for nozzle with D_o=0.8 mm, H=1.13 mm and Θ=45^o with applied pressure and pressure ratio of (a)2 kPa and 1.67 (b) 3 kPa and 2.50 (c) 4 kPa and 3.33. Scale bars: 1 mm.

Figure A.7a shows the iteration for an increasing outer wall angle. The lower wall angles don't perform well at 18 mL/min whereas the nozzles with higher wall angles do seem to produce snaking and multidisperse bubbles. At higher liquid flow rates all nozzles perform similar. The lower angle might be obstructing liquid flow and causing some instabilities which result in unusable phases. The data points are relatively scarce and not much more can be said. This will have to be verified using either visual or numerical testing.

In figure A.8a the nozzle iteration for decreasing outer nozzle diameter is shown. The relation to the modelled transition pressure is clear. As the pressure data points become more coarse at higher data pressures, it is difficult to say how the nozzles compare to one another. We do see the first instances of monodisperse bubbles created with the nozzles in the experiments which are shown in figure 4.10.

The results of the iteration of the outer nozzle diameter with constant height between inner and outer nozzle are shown in figure A.9a. These results are similar to the results in figure A.8a but overall it appears that fewer points lie in the snaking, mono- or multidisperse bubble phase. This might be because the longer height which is apparent in the changing height iteration, causes less obstruction to the liquid flow and thus allow it to flow more freely and allow for usable phases. This phenomenon of larger height between both nozzles allowing more usable phase is also visible in the

Table 4.2: Design table of nozzle geometries for the first design iteration.

Nozzle No.	D_o [mm]	H [mm]	\theta [^{o}]
103	0.8	0.93	45
100-105	0.8	0.73-1.13	45
106-111	0.8	0.93	25-50
112-116	0.5-1.0	0.83-1.08	45
117-121	0.5-1.0	0.93	45

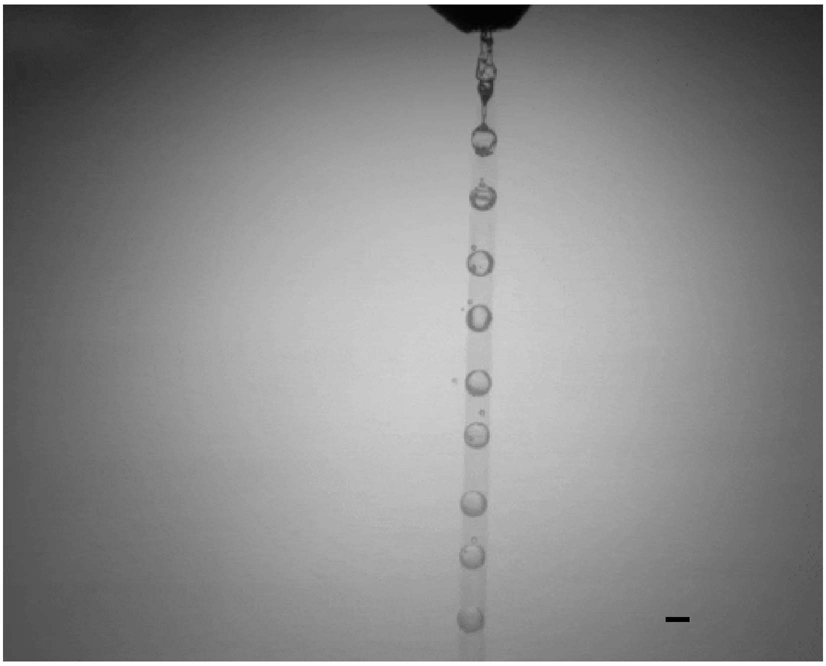

Figure 4.10: First observation of monodisperse bubbles (D_o=0.5 mm, H=1.08 mm and Θ=45^o). Scale bar: 1 mm.

distance between inner and outer nozzle iteration.

Dimensionless plots for nozzles without a throat section and changing height, outer wall angle and outer diameter

When comparing the phase diagrams of the nozzles without throat section to figures A.2 through A.5, it is clear that for the same pressure and liquid flow rates more usable phases are obtained. Similar to the first data set, the dimensionless plot is made by using the measured outer diameter and modelled inner dimensions to calculate a transition pressure and Weber number for all experiments. This plot is shown in figure 4.11.

Additional experiments have been performed in order to make the figure more complete. The transition from dripping to jetting was not seen in figure 4.8 and also no transition from dripping to the build-up phase. Data points with Weber numbers ranging from 0.6 to 15 were prepared and the lower limit of the pressure controller range was used as the lowest pressure of a pressure set ranging from 600 to 1800 Pa. There were also few results in the monodisperse region and these are expected to be found for $We \approx 30$ and $P/P_{tot} \approx 1$. A higher Weber number means a higher liquid velocity when using the same liquid. When using a smaller outer nozzle, the liquid velocity is higher for a given liquid flow rate. Having a lower liquid flow rate means that more experiments can be carried out without filling the syringes and therefore some of the smaller nozzles from the second nozzle set have been used. Liquid flow rates were calculated to result in Weber number ranging between 20 and 50 with 4 values logarithmically spaced for all three nozzles. The transition pressure was calculated for these liquid flow rates and the pressure was calculated to have a pressure ratio between 0.7 and 1.5 in 5 steps. Higher pressure ratios was not deemed necessary since the spray markers already encapsulate the top part of the figure.

The results of the first design iteration show a clear distinction between phases. For Weber numbers below 4 a transition from dripping to build-up is observed for increasing pressure ratio. This

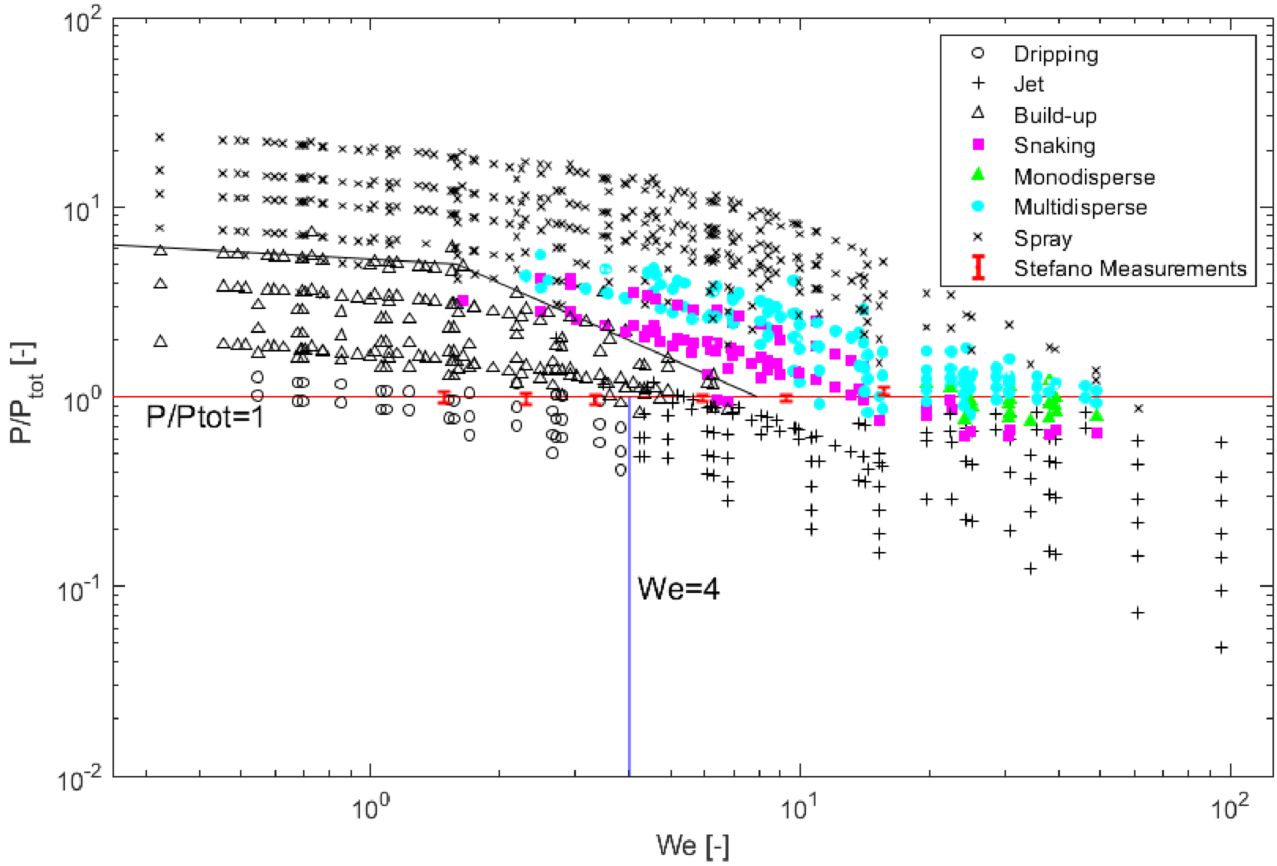

Figure 4.11: The dimensionless pressure ratio as a funciton of the Weber number and the resulting phase for the first design iteration.

build-up transitions to spray for low Weber number and for higher Weber number also a transition from build-up to snaking and multidisperse bubbles to spray is observed. The build-up regiun has been marked off with a black line which is meant as a guide for the eye and does not yet have physical meaning. The transition from dripping to jetting for increasing Weber number below the transition pressure has been marked with a blue line which is placed at the previously found $We > 4$. As mentioned previously this is due to the inertial forces overcoming the surface tension forces and this is visible in figure 4.12. For $We < 4$ the surface tension forces are dominant and incoming liquid adheres to the nozzle and to itself. For a slightly higher Weber number the kinetic forces become dominant and a liquid column is formed which still adheres somewhat to the nozzle. For a higher Weber number the kinetic forces are dominating and the result is a liquid jet which does not adhere to the nozzle sides but is ejected from the nozzle continuously.

When looking at the region where the experiments were done which aimed at further identifying the monodisperse bubble region, it can be seen that a lot more experiments resulting in the monodisperse bubble phase were obtained. In figure 4.13 the focus is on the monodisperse region. These appear mainly for Weber numbers ranging from 25 to 40 and pressure ratios from 0.8 to 1. The snaking phase is also observed as a separate region. For increasing Weber number this transitions to multidisperse bubbles. For higher pressure ratios the spraying phase is found for all values of Weber number.

In figure 4.13 a trend is observed where with increasing pressure ratio jetting turns to snaking which turns to monodisperse bubbles which then turns to multisdisperse bubbles which turn to spray.

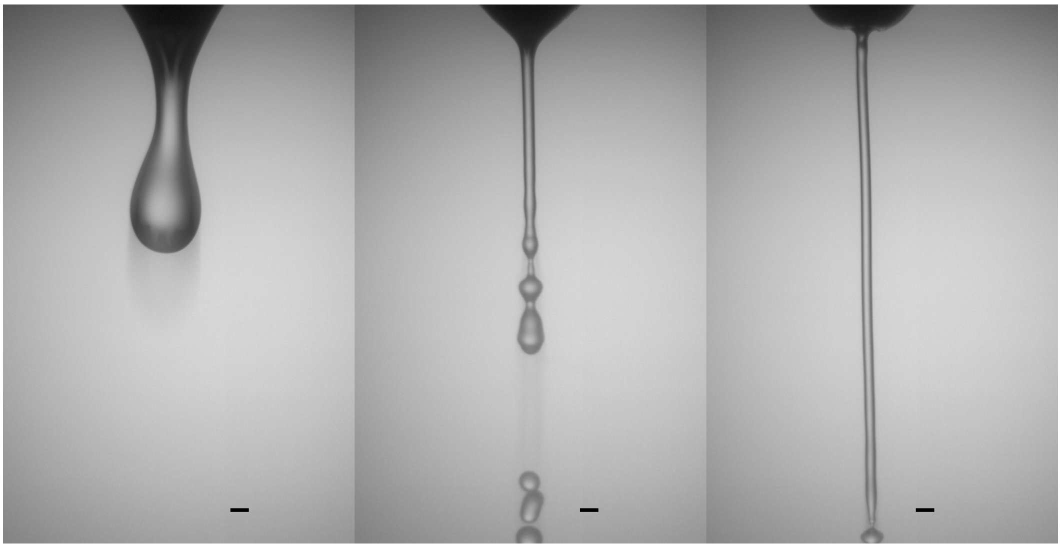

Figure 4.12: Transition from dripping to jetting for increasing Weber number of 3.8, 6.7 and 15.3, respectively and below the pressure transition line. Scale bars: 1 mm.

The instances of snaking were often similar to jetting but with some encapsulation of air. This is observed in the transition in figure 4.14. It can be seen that the ejecting liquid does not adhere to the nozzle which can be explained with the Weber number being higher compared to the jet in figure 4.12. This separation of liquid from the nozzle might allow the bubbles to also separate from themselves and allows the formation of monodisperse bubbles and this may be the reason why monodisperse bubbles only form at higher Weber number. In figure 4.15 it can be seen that for some snaking phases the liquid does adhere to the nozzle. This does not hold for all snaking phase though as can be seen in the final picture in figure 4.15. The snaking phases at higher Weber number are becoming more sparse and as can be seen in figure 4.14, the snaking phase does resemble jetting except for some gas encapsulation. There is some relation with the inertial forces although it can't be certain until some additional visual and numerical simulation tests are done.

4.2.3 Discussion

There is an offset of the transition from dripping to build-up from the transition pressure line in the lower Weber numbers and this can be partly explained. For lower Weber number the capillary pressure and pressure drop due to friction become dominant. The inner nozzle diameter was not accurately measured using a microscope for all nozzles and therefore an average value for the inner nozzle radius was used to calculate the capillary pressure. Also the pressure controller already measured 120 Pa at ambient pressure when no liquid was supplied to the nozzle. This is within the accuracy error of ± 150 Pa of the pressure controller, but this pressure offset was repeatably measured. The instances of monodisperse bubble formation were mainly observed for Weber numbers ranging from 25 to 40 and a pressure ratio between 0.8 and 1. With a pressure ratio lower than 1 no gas introduction is expected but this means that the modelled transition pressure slightly overestimates the actual transition pressure or the measured outer nozzle diameter is not accurate. The higher Weber numbers are represented by the smaller outer nozzle diameters since these have higher liquid velocity for a given liquid flow rate compared to larger outer nozzle diameters. The measurements of the nozzle diameters were less accurate for the smaller diameters since these showed more deviations from a circle as shown in figure 3.13. This inaccuracy will have some impact on the

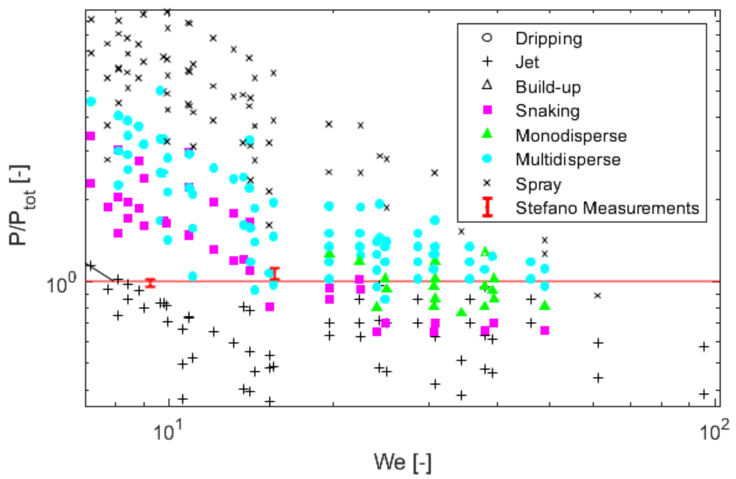

Figure 4.13: Zoomed portion of the dimensionless plot focusing on the monodisperse region.

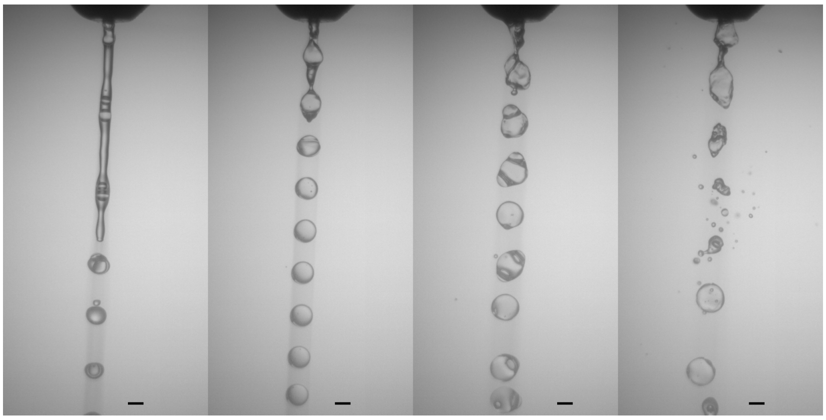

Figure 4.14: Resulting phase transition for $We = 26.5$ and pressure increasing from 0.7 to 0.86, 1.18, 1.5. Scale bars: 1 mm.

results since a larger effective area will cause a lower liquid velocity and thus a lower Weber number and a lower modeled transition pressure and thus a higher pressure ratio.

The shown Weber number in the dimensionless plots is not accurate when gas is introduced in the ejection phase. Gas will also travel through the nozzle effectively decreasing the area through which the liquid is flowing. This will cause an increase in the liquid's velocity as shown in figure 2.5b. For now this can't be taken in to account since the flow rate of gas is unknown since only the gas pressure is used as a controlling parameter. A higher pressure ratio will cause a larger gas flow and this will cause a higher liquid velocity. Already some influence of the gas pressure to the ejecting velocity has been investigated in previous research by high speed imaging analyses so this could be done for a more accurate representation of the dimensionless plot [12].

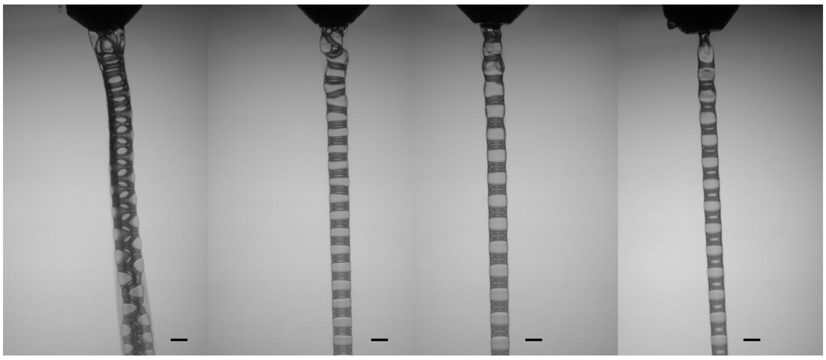

Figure 4.15: Observed snake phases for Weber number being 3.2, 4.3, 7.7 and 10.9, respectively. Scale bars: 1 mm.

Chapter 5

Conclusions and recommendations

5.1 Conclusions

This thesis presents the development of a 3d foam printer platform and an investigation into the effect of the coaxial nozzle geometry on the resulting ejection phase at varying ink flow rate and gas pressure. The required components and requirements for an actuation were constructed and from offers from several suppliers, a package containing linear motors, servo drives and a motion controller was chosen. This is mounted on a heavy granite base to reduce vibrations which is supported by pneumatic dampeners and an aluminium frame. This set-up allows for accurate and fast actuation in order to 3d print foams. Other extrusion based processes could also be mounted on the set-up to make geometric shapes.

Based on previous research a nozzle design was acquired and several iterations resulted in a set of design rules of the geometry for the production process. This showed that the resulting resolution of the process limited the available design space. Within this design space the influence of the nozzle geometric parameters was investigated.

Two nozzle sets were designed from a base nozzle with iterations of the inner and outer nozzle diameter, the outer wall angle, the distance between inner and outer nozzle and the presence of a nozzle throat. These nozzles were produced and mounted in the set-up and the resulting ejection phase was observed for an ink flow rate of [8 12 18 24 30] mL/min and a gas pressure of [1 2 3 4 6 8 12] kPa. These results were compared using phase diagrams which mapped the resulting phase at varying ink flow rate and pressure. It was found that the outer wall angle and inner nozzle diameter had little influence on the resulting ejecting phase unless the distance between inner and outer nozzle became critically small. There was a clear correlation between the outer nozzle diameter and the pressure at which gas was introduced into the ejection phase which was confirming previous research. The distance between inner and outer nozzle also had a significant effect on the resulting ejection. A small distance was not possible due to clogging of the nozzle and for too large distance only spraying was observed. To allow for a smaller distance, the throat section was discarded in the model and this resulted in more stable ejection with also the formation of monodisperse bubbles.

A model for the transition pressure was previously presented and this was used to scale the pressure data points. The Weber number was used to visualize the liquid velocity. In the resulting plots distinct regions were observed for various ejection phases. During processing of the data it was found that there was insufficient data for low pressure ratio and low Weber number. For this cause additional experiments have been carried out to map the transition from dripping to jetting and the transition from dripping to the build-up phase. The transition from dripping to jetting for $We > 4$ corresponds nicely with literature. The transition to build-up has an offset from the modeled transition pressure which is more relevant for lower Weber number so there is some static effect which could be better described.

Also additional experiments have been performed in the region in which monodisperse bubbles were observed. In order to gain more knowledge in this region, more experiments were prepared with a Weber number ranging from 20 to 50 and a pressure ratio between 0.7 and 1.5, These show monodispere bubbles for a Weber number between 20 and 50 and a pressure ratio between 0.8 and 1.1. These values can be used for newly produced nozzles or other liquids with different properties and therefore reduce the need for doing additional experiments in order to derive the ejection phases at varying liquid flow and gas pressure.

5.2 Recommendations

In the experiments a pressure controller was used and therefore no insight is gained in the actual gas flow. When gas is introduced into the ejecting flow the liquid will effectively have a smaller area through which it is passing. The actual liquid velocity is therefore higher than was modelled in the dimensionless plots for increasing pressure ratio above the transition pressure. For this purpose a flow meter could be used in order to be able to better approximate the conditions to get a more accurate dimensionless ejection characterization at higher pressure ratios.

The accuracy of the nozzle production was limited in this research. Despite being an accurate way of 3d printing, the SLA machine was a relatively cheap desktop printer available at the university. This did mean that alterations to the model were necessary but new batches could be made quickly and cost effectively. In order to scale down the model or investigate other configurations like having both nozzles in one plane, it is necessary to investigate other production methods like glass etching or 2-photon polymerization. The change in surface roughness of the produced nozzles might also have a noticeable effect on the ejection.

The used flow meter was not able to control a sufficiently low pressure for all used liquid flow rates in the dripping region. Despite this fact, the transition from dripping to build-up was noticed in the experiments. When using other liquids it should be checked whether the used pressure controller has a sufficient range for the nozzles which are used in the process.

In order to better understand the ejection phases it is beneficial to use a high speed camera. From the displacement between frames, the velocity can be acquired and the total volume flow can be calculated with some post-processing of the images. Using this data the dimensionless plot can be made with better approximation of the Weber number.

Further research should be done on actually producing polymer foams in three-dimensional shapes using the newly acquired set-up. These shapes should further show the possibilities and limitations of the process. On this set-up it can also be verified whether using the snaking phase as shown in figure 4.3d also results in usable foam parts which fully polymerize.

Numerical simulations on the fluid dynamics within the nozzle could further explain the observed ejection regions and this insight can be used to further optimize a nozzle design. The results from this thesis can be used as a way of verifying simulation results.

Bibliography

[1] S. Andrieux, A. Quell, C. Stubenrauch, and W. Drenckhan, "Liquid foam templating A route to tailor-made polymer foams," *Advances in Colloid and Interface Science*, vol. 256, no. 2017, pp. 276–290, 2018. [Online]. Available: https://doi.org/10.1016/j.cis.2018.03.010

[2] C. Stubenrauch, A. Menner, A. Bismarck, and W. Drenckhan, "Emulsion and Foam Templating-Promising Routes to Tailor-Made Porous Polymers," *Angewandte Chemie - International Edition*, vol. 57, no. 32, pp. 10 024–10 032, 2018.

[3] S. Berezvai and A. Kossa, "Effect of the skin layer on the overall behavior of closed-cell polyethylene foam sheets," *Journal of Cellular Plastics*, vol. 52, no. 2, pp. 215–229, 2016.

[4] U. G. Wegst, "Bending efficiency through property gradients in bamboo, palm, and wood-based composites," *Journal of the Mechanical Behavior of Biomedical Materials*, vol. 4, no. 5, pp. 744–755, 2011. [Online]. Available: http://dx.doi.org/10.1016/j.jmbbm.2011.02.013

[5] S. Mannan, M. Zaffar, A. Pradhan, and S. Basu, "Measurement of microfibril angles in bamboo using Mueller matrix imaging," *Applied Optics*, vol. 55, no. 32, p. 8971, 2016.

[6] E. R. Fotsing, A. Dubourg, A. Ross, and J. Mardjono, "Acoustic properties of a periodic micro-structures obtained by additive manufacturing," *Applied Acoustics*, vol. 148, pp. 322–331, 2019. [Online]. Available: https://doi.org/10.1016/j.apacoust.2018.12.030

[7] B. Huang, C. Vyas, I. Roberts, Q. A. Poutrel, W. H. Chiang, J. J. Blaker, Z. Huang, and P. Bártolo, "Fabrication and characterisation of 3D printed MWCNT composite porous scaffolds for bone regeneration," *Materials Science and Engineering C*, vol. 98, no. December 2018, pp. 266–278, 2019. [Online]. Available: https://doi.org/10.1016/j.msec.2018.12.100

[8] B. P. Chan and K. W. Leong, "Scaffolding in tissue engineering: General approaches and tissue-specific considerations," *European Spine Journal*, vol. 17, no. SUPPL. 4, 2008.

[9] P. F. Egan, I. Bauer, K. Shea, and S. J. Ferguson, "Mechanics of Three-Dimensional Printed Lattices for Biomedical Devices," *Journal of Mechanical Design*, vol. 141, no. 3, p. 031703, 2018.

[10] L. G. Bracaglia, B. T. Smith, E. Watson, N. Arumugasaamy, A. G. Mikos, and J. P. Fisher, "3D printing for the design and fabrication of polymer-based gradient scaffolds," *Acta Biomaterialia*, vol. 56, pp. 3–13, 2017. [Online]. Available: http://dx.doi.org/10.1016/j.actbio.2017.03.030

[11] W. Drenckhan and D. Langevin, "Monodisperse foams in one to three dimensions," *Current Opinion in Colloid and Interface Science*, vol. 15, no. 5, pp. 341–358, 2010. [Online]. Available: http://dx.doi.org/10.1016/j.cocis.2010.06.002

[12] S. Coco, “Faculty of Science and Technology Direct Bubble Writing : a new Additive Manufacturing technology for 3D printing foams,” pp. 1–40, 2018.

[13] Ultimaker. Mastering cura. [Online]. Available: https://ultimaker.com/en/resources/21932-mastering-cura

[14] R. Blake, *Harris’ Shock and Vibration Handbook Chapter 2: Basic Vibration Theory*, 2007.

[15] J. Schilder, “Dictaat 066, dynamics 2,” 2015.

[16] S. Kleiven, P. Halldin, and D. Zenkert, “Dynamic Finite Elment Methods, Lecture Notes for 4E1150,” pp. 1–29, 2001.

[17] I. Gibson, D. Rosen, and B. Stucker, *Additive Manufacturing Technologies*, 2015.

[18] V. S. Voet, T. Strating, G. H. Schnelting, P. Dijkstra, M. Tietema, J. Xu, A. J. Woortman, K. Loos, J. Jager, and R. Folkersma, “Biobased Acrylate Photocurable Resin Formulation for Stereolithography 3D Printing,” *ACS Omega*, vol. 3, no. 2, pp. 1403–1408, 2018.

[19] F. support. Choosing the right material. [Online]. Available: https://support.formlabs.com/s/article/Choosing-the-Right-Material?language=en_US

[20] Formlabs. Design specs form 2. [Online]. Available: https://formlabs.com/3d-printers/form-2/design-specs/

[21] Materialise. Design guidelines - tuskxc2700w - stereolithography. [Online]. Available: https://www.materialise.com/en/manufacturing/materials/tuskxc2700w/design-guidelines

[22] D. hubs. Design rules for 3d printing. [Online]. Available: https://www.3dhubs.com/get/3d-printing-design-rules/

[23] M. Parhizkar, M. Edirisinghe, and E. Stride, “The effect of surfactant type and concentration on the size and stability of microbubbles produced in a capillary embedded T-junction device,” *RSC Advances*, vol. 5, no. 14, pp. 10 751–10 762, 2015.

[24] A. Bąk and W. Podgórska, “Interfacial and surface tensions of toluene/water and air/water systems with nonionic surfactants Tween 20 and Tween 80,” *Colloids and Surfaces A: Physicochemical and Engineering Aspects*, vol. 504, pp. 414–425, 2016.

[25] D. Vidanovic, J. Milic Askrabic, M. Stankovic, and V. Poprzen, “Effects of nonionic surfactants on the physical stability of immunoglobulin G in aqueous solution during mechanical agitation,” *Pharmazie*, vol. 58, no. 6, pp. 399–404, 2003.

[26] Shodhanga, “CHAPTER - VI ULTRASONIC , VISCOSITY AND REFRACTOMETRIC STUDIES ON TWEEN-20 / WATER AND TWEEN-80 /.”

[27] M. Versluis, “High-speed imaging in fluids,” no. February 2013, 2017.

[28] W. van Hoeve, S. Gekle, J. H. Snoeijer, M. Versluis, M. P. Brenner, and D. Lohse, “Breakup of diminutive Rayleigh jets,” *Physics of Fluids*, vol. 22, no. 12, pp. 1–11, 2010.

[29] R. L. M. T. Collins. (2015) A selection guide for linear systems. [Online]. Available: https://www.linearmotiontips.com/selection-guide-linear-systems/

[30] C. M. Layosa. (2015) Strengths and limitations: Belt drive vs ball screw actuators. [Online]. Available: http://blog.misumiusa.com/strengths-limitations-belt-drive-vs-ball-screw-actuators/

[31] E. linear motors. (2018) What is a linear motor - principle. [Online]. Available: https://www.etel.ch/linear-motors/principle/

Appendix A

Phase diagrams

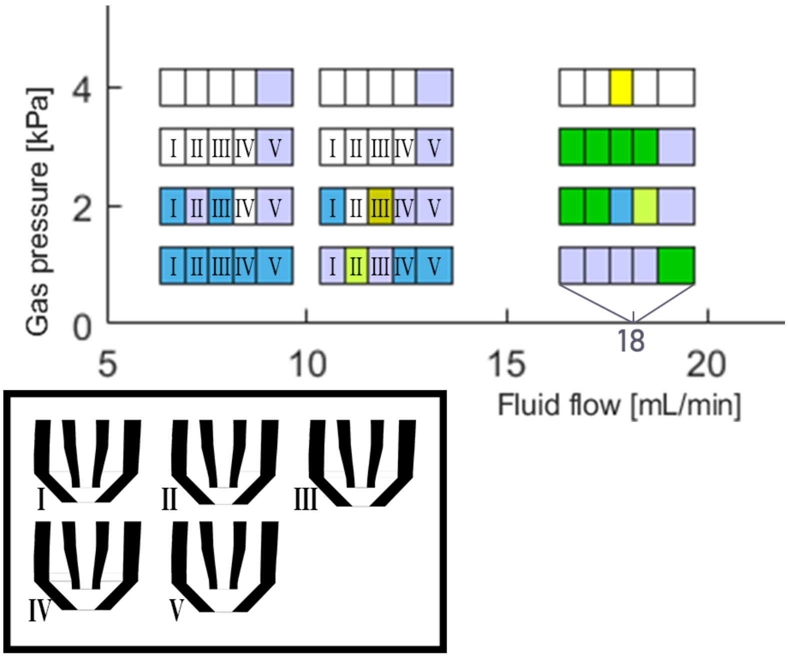

Figure A.1: Explanation on phase diagram structure

The composition of phase diagrams for several nozzle iterations is visible in figures A.2a through A.9a. A short explanatory figure is shown in figure A.1. Here it is shown how the phase diagram shows five successive nozzles within a parameter iteration. These nozzles correspond to the horizontally connected squares denoted with the Roman numerals. The column on the right shows that all of these data points of the entire column share a fluid flow rate of 18 mL/min.

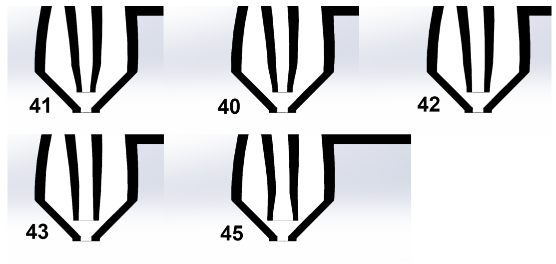

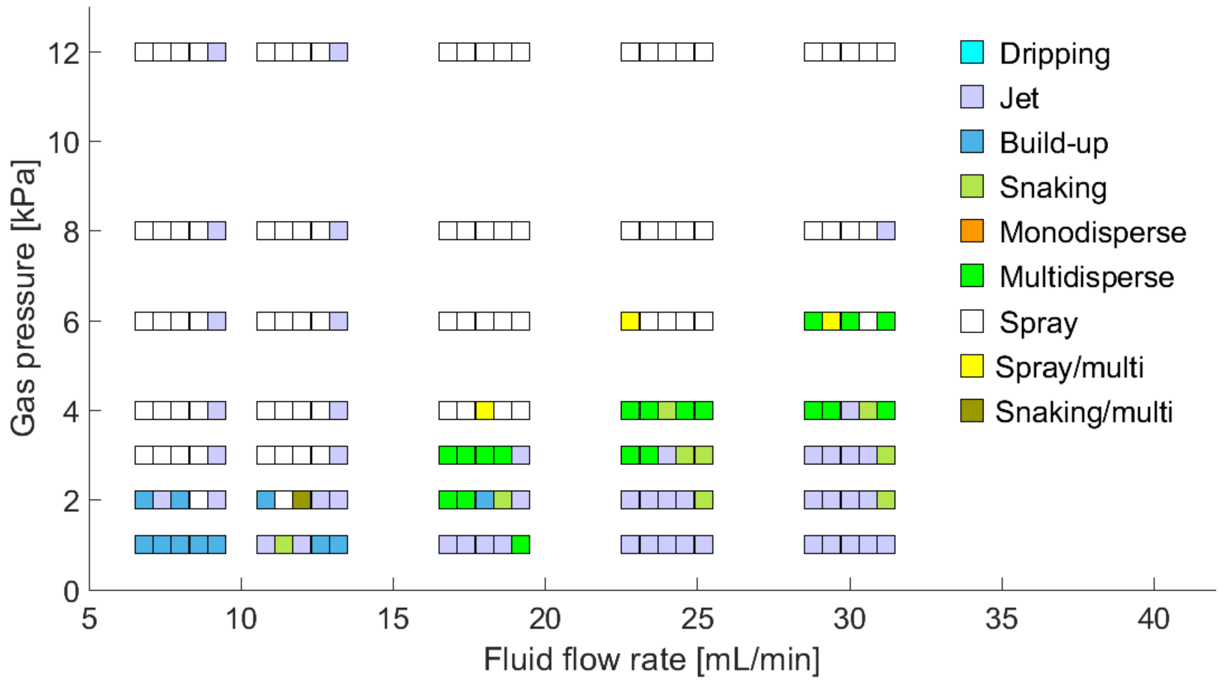

Figure A.2: Nozzle set which shows the nozzles with increasing inner nozzle diameter and resulting phase diagram. Nozzle control parameters: D_i=0.6-1.5 mm, D_o=0.8 mm, H=1.5 mm, Θ=45^o.

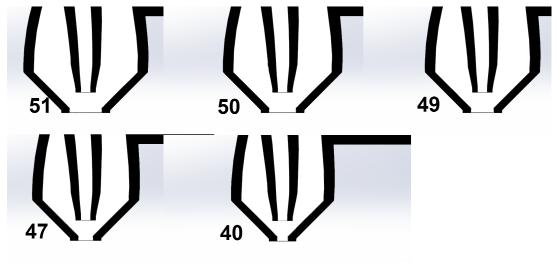

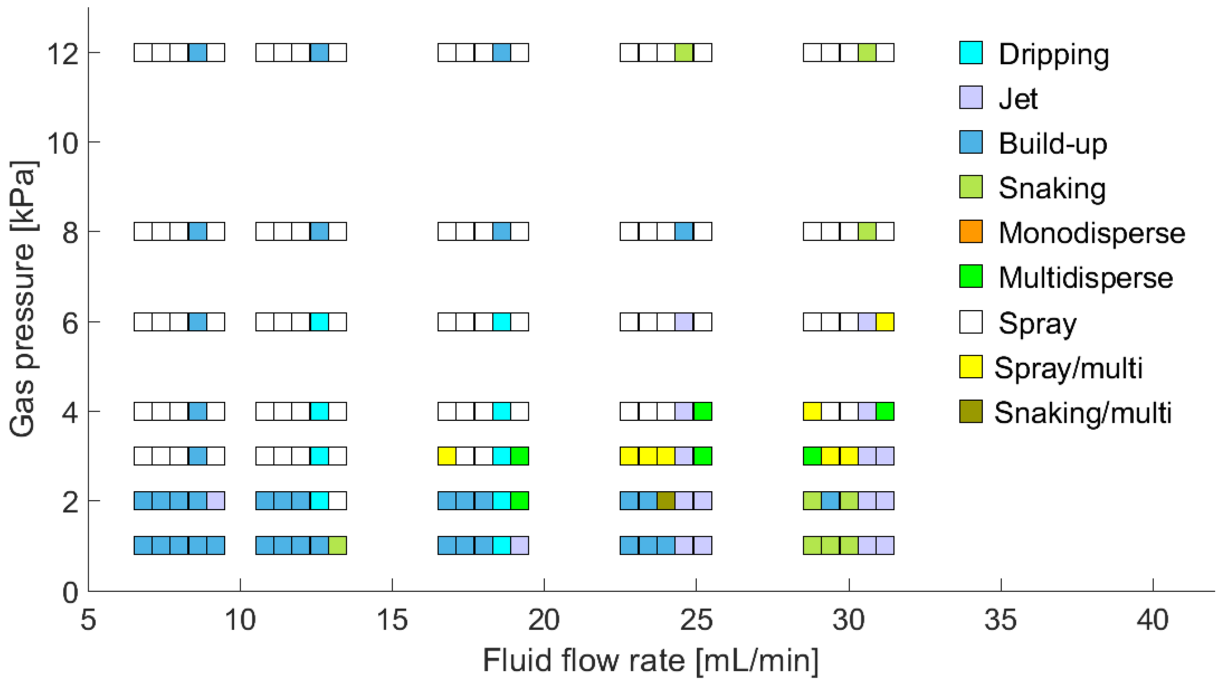

Figure A.3: Nozzle set which shows the nozzles with decreasing outer nozzle diameter and resulting phase diagram. Nozzle control parameters: D_i=0.7 mm, D_o=0.8-2.4 mm, H=1.5 mm, Θ=45^o.

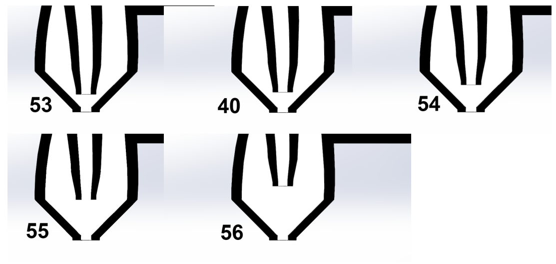

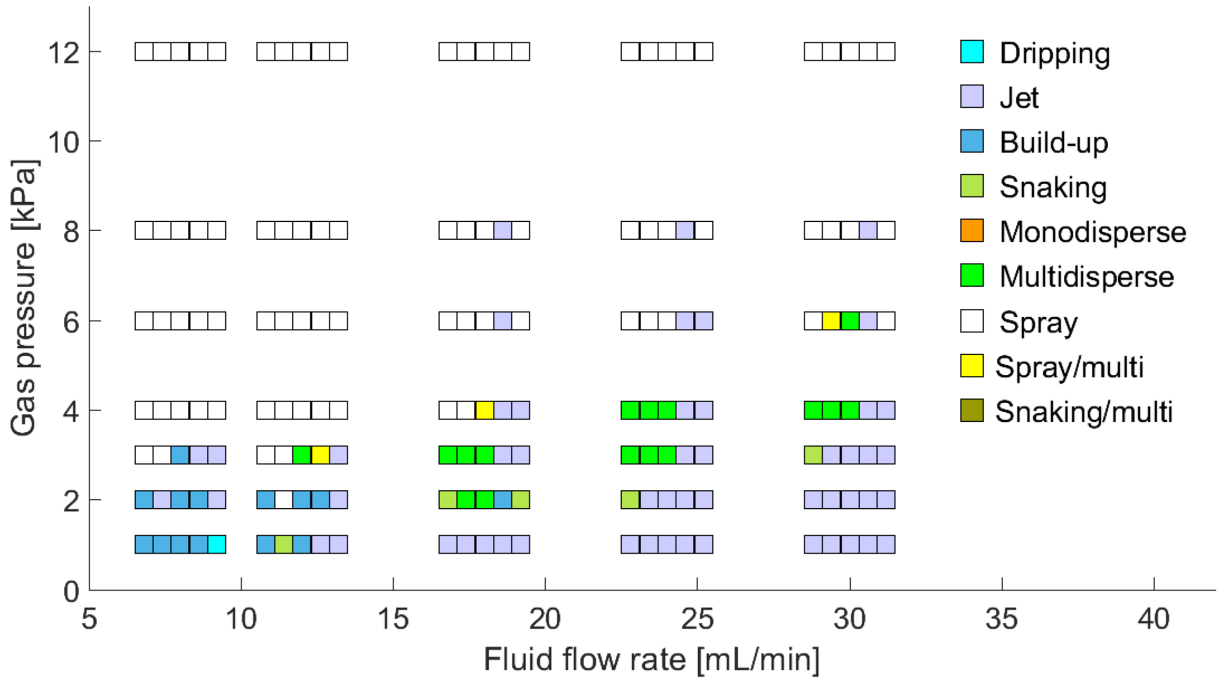

Figure A.4: Nozzle set which shows the nozzles with increasing distance between inner and outer nozzle and resulting phase diagram. Nozzle control parameters: D_i=0.7 mm, D_o=0.8 mm, H=1.3-4 mm, Θ=45^o.

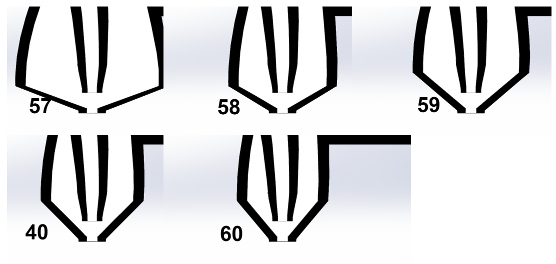

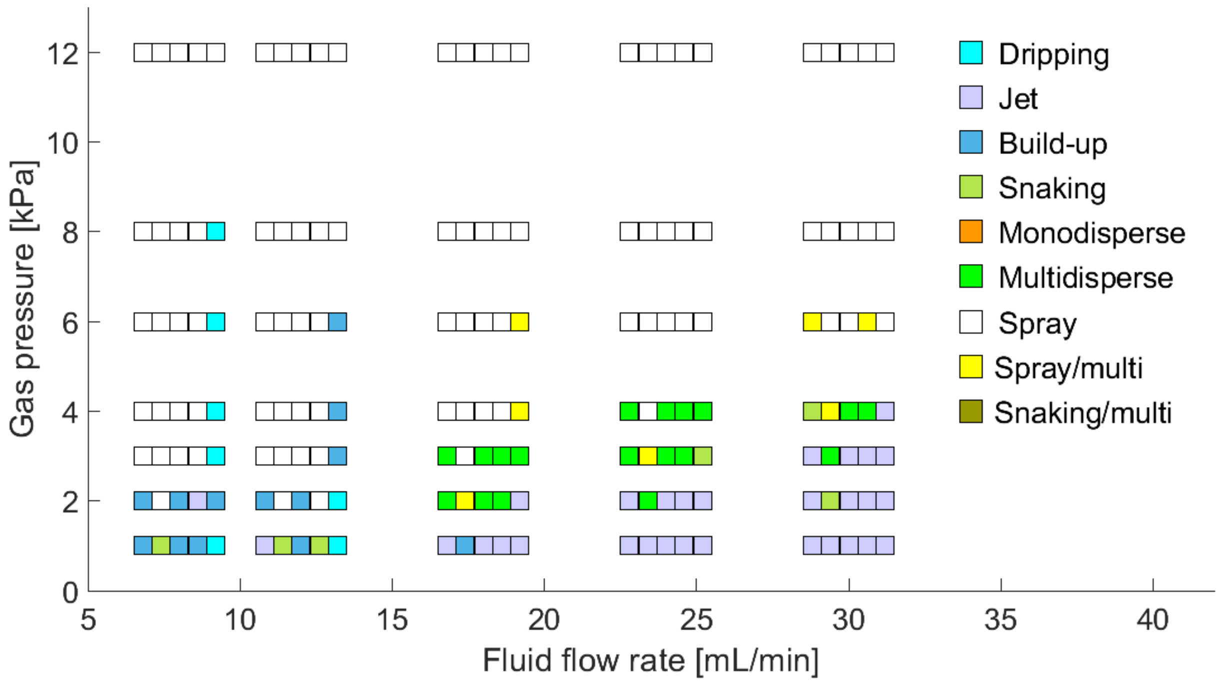

Figure A.5: Nozzle set which shows the nozzles with increasing outer wall angle and resulting phase diagram. Nozzle control parameters: D_i=0.7 mm, D_o=0.8 mm, H=1.5 mm, Θ=20-50^o.

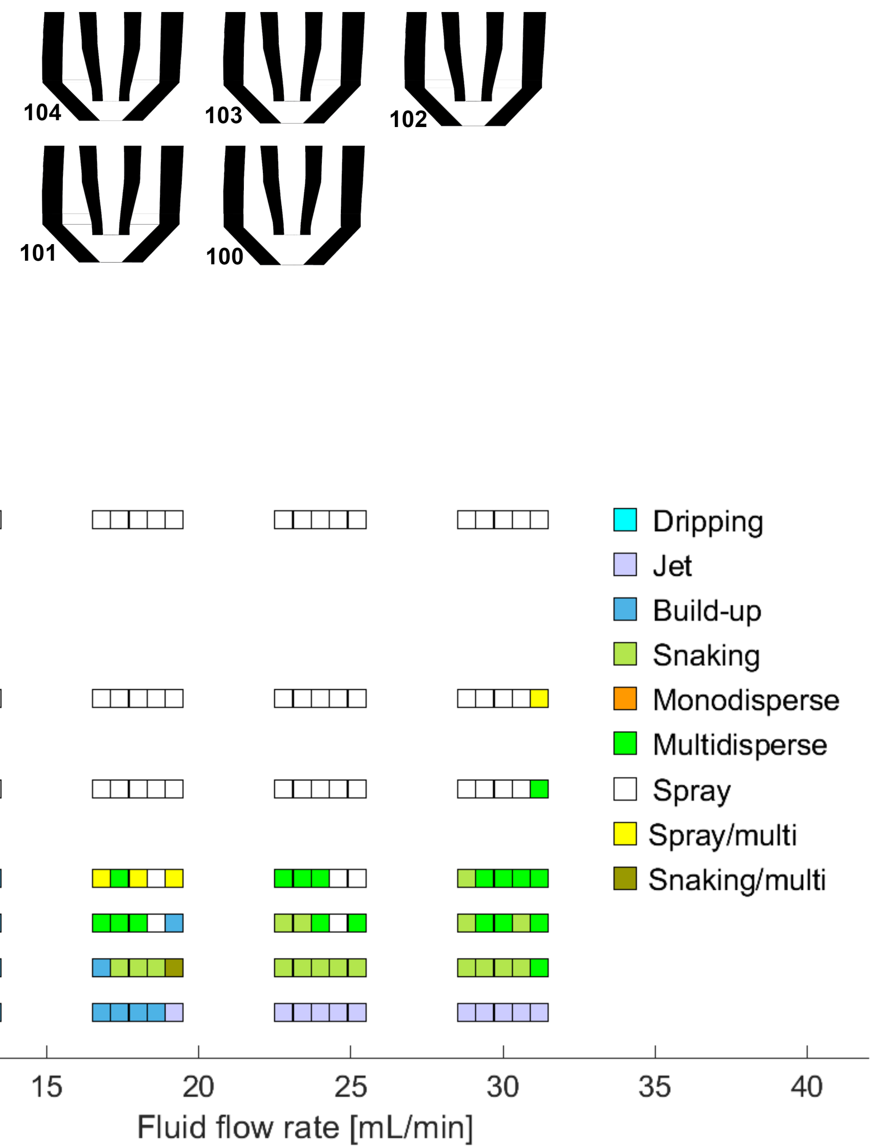

Figure A.6: Nozzle set which shows the nozzles without throat with increasing distance between inner and outer nozzle and resulting phase diagram. Nozzle control parameters: D_o=0.8 mm, H=0.73-1.13 mm, Θ=45^o.

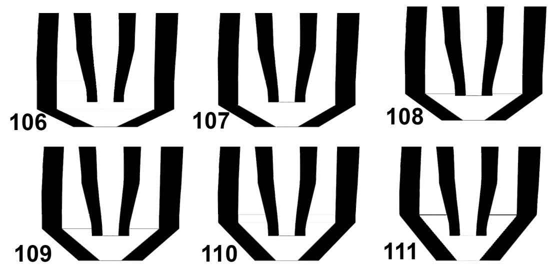

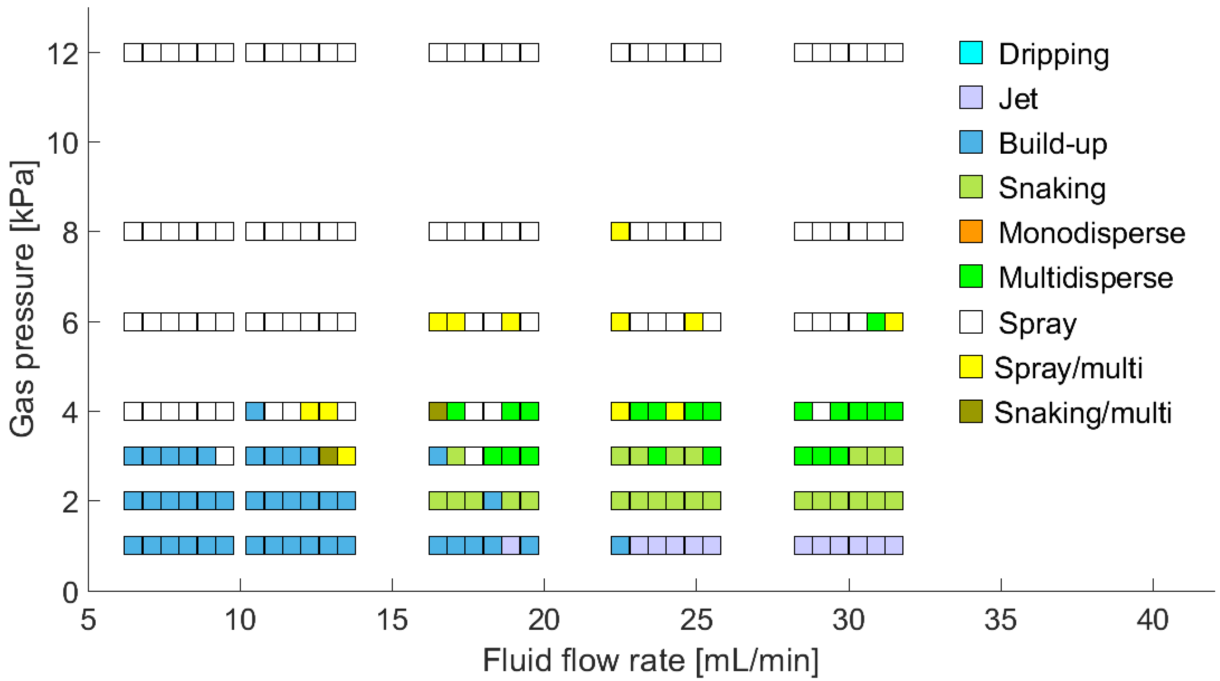

Figure A.7: Nozzle set which shows the nozzles without throat with increasing outer wall angle and resulting phase diagram. Nozzle control parameters: D_o=0.8 mm, H=0.93 mm, Θ=25-50^o.

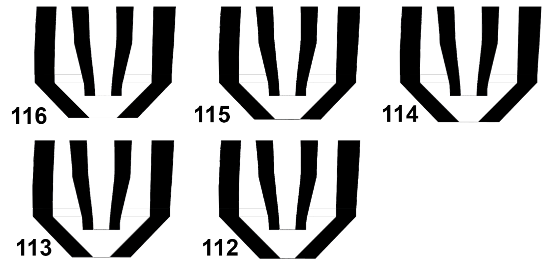

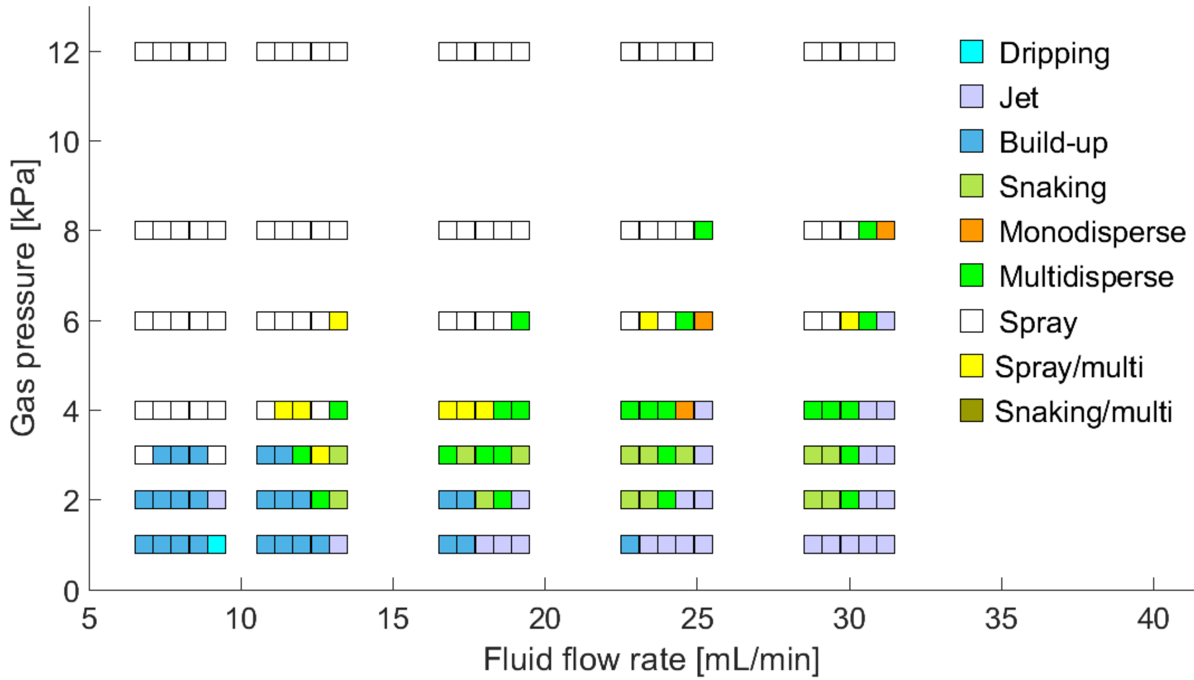

Figure A.8: Nozzle set which shows the nozzles without throat with decreasing outer nozzle diameter with changing distance between inner and outer nozzle and resulting phase diagram. Nozzle control parameters: D_o=1-0.5 mm, H=0.83-1.08 mm, Θ=45^o.

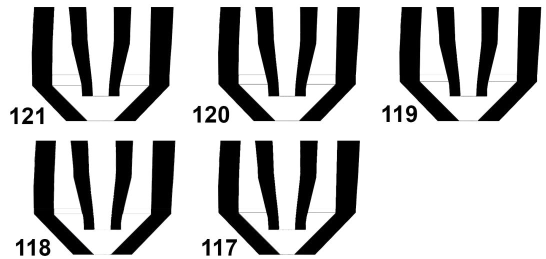

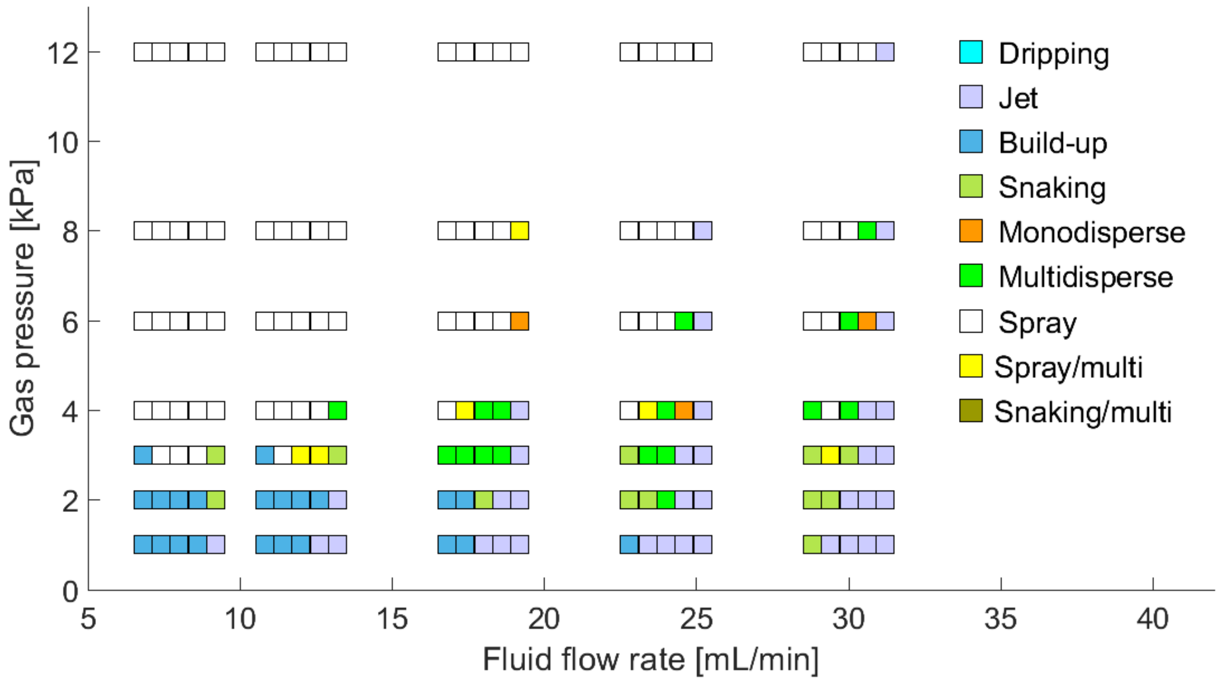

Figure A.9: Nozzle set which shows the nozzles without throat with decreasing outer nozzle diameter with constant distance between inner and outer nozzle and resulting phase diagram. Nozzle control parameters: D_o=1-0.5 mm, H=0.93 mm, $\Theta=45^o$.

Appendix B

Selection of drive mechanism

A positioning system uses a drive mechanism to actuate the end effector. There are several options which would fit this set-up. For this set-up with aforementioned requirements belt driven systems, ball screw driven systems and linear motors are compared.

B.0.1 Belt driven system

A belt driven system converts the rotary motion of a servo motor to linear motion of the carriage using a timing belt. Belt driven systems are capable of traversing long lengths at high speeds. This system has few moving parts which makes for less maintenance required, besides periodically re-tensioning of the belts. Because of elongation of the rubber belt at higher loads and lengths, belt driven systems have a lower repeatability and travel accuracy compared to other drive mechanisms. Also resonance due to the elasticity of the belt, causes the system to have higher settling times [29], [30].

B.0.2 Ball screw

A ball screw is an improved version of a lead screw driven system. The rotary motion of a servo motor rotates a lead screw. The carriage is actuated linearly by this rotation using a ball bearing system. Using pre-loaded nuts backlash-free motion can be achieved. Because of the ball bearing system, higher loads and thus acceleration and accuracy are possible. This mechanism is limited in its travel length and velocity and is more expensive than the belt driven systems [29], [30].

B.0.3 Linear motor

Linear motors work using the interaction of a coil assembly and a permanent magnet assembly. The carriage is directly coupled to the machine load which eliminates backlash, simplifies the design and removes failure sources from mechanical transmissions. These systems offer high speed and high acceleration capacities at high accuracy and the simple design requires less maintenance. Traditionally these systems are very costly [29], [31].

B.0.4 Offers and choice

Several companies were contacted and the resulting offers are shown in Table B.1. VarioDrive offered a solution which incorporated pre-tensioned ball screws. Groneman uses tubular linear motors and the rest of the offers use conventional linear motors. Based on the requirements the second

Table B.1: [1] Entire set-up including granite base and frame
[2] Actuators, servo controllers and motion controller
[3] Actuators and servo controllers. No motion controller

Company	Accuracy (repeatablity) [μm]	Velocity [mm/s]	Acceleration [m/s^2]	Price [Euro]
Physik Instrumente	0.5	500	10+	100,000.00[1] 50,000.00[2]
VarioDrive	3 per axis	1200	20	37,535.00[2]
Groneman	10	500	10-20	20,600.00[3]
ATB Automation	1-10 20	500 1000	10 4	22,098.00[2] 17,000.00[2]

offer of ATB Automation was discarded. It was desirable that the solution was as complete as possible while still being affordable. The solution from Groneman required a motion controller from an additional supplier. This could cause additional problems regarding compatibility and communication with additional parties. The offer from Groneman was therefore discarded. The price difference in the remaining offers was substantial and since all offers satisfy the requirements, the offer from ATB Automation is chosen.

B.1 Resulting set-up

A model of the resulting set-up is shown in figure 3.3b. This shows a heavy granite base which reduces vibrations due to its mass and due to its porosity. This is mounted to an aluminium frame using pneumatic vibration dampeners which prevent vibrations from outside entering the system and vice versa. The axes are driven by servo drives supplied by ATB Automation. These have an internal control loop with feedback from a submicron linear encoder. The control of the servo drives is done through a Trio motion controller. The motion profile of the print head can be done in several ways and there are some commands for having continuous motion through corner rounding or drawing a spline through position points which is interesting for the continuous ejection of direct bubble writing. The communication of the motion controller and connected PC is done through the EtherCAT protocol. This is a simple and fast method of connecting industrial applications through Ethernet cables. The pressure controller can also communicate through EtherCAT and can therefore be directly implemented in the programming of shapes.
The fact that the individual linear axes are mounted in series has allowed a lower price, but in order to have sufficient stiffness, a lot of mass had to be added in the form of supporting structure. It is therefore interesting to see how the structure performs in terms of deflection and vibration. The supplier does not perform these simulations and therefore a small study has been made in section 3.2.

Appendix C

UV radiation control

In order to initiate the polymerization process, the ink is exposed to UV radiation. The photoinitiator used is Omnirad BDK, also known as Irgacure 651. In C.1 the absorbance for this photoinitiator is shown. Affordable UV LEDs emit UV radiation at wavelengths ranging from 365 nm to 400 nm. In this range the photoinitiator absorbs more of the UV radiation at a shorter wavelength and therefore SMB1N-365V-02 LEDs have been chosen which emit at 365 nm. These LEDs can emit up to 500 mW of power each so this radiated power can be tuned to give the best results. The LEDs are placed around the nozzle to get a homogeneous illumination of the bubble in the air and after impact. The placement and angle of the LEDs determines the illuminated area of the bubble and the duration of this illumination. A short study is shown in figure C.2. It can be seen that having the LEDs closer to the nozzle, makes for a smaller illuminated area for a longer period of time. In the set-up the influence of this placement will be tested and in order to accomplish this, an array was modelled and produced using FDM 3d printing. In this design special care was taken to ensure that the LED rays were in line with the nozzle which is mounted in the center. For the LEDs a bracket was modelled and similarly produced. These brackets are mounted using nuts and bolts and the angle of each bracket can be alternated using this connection.

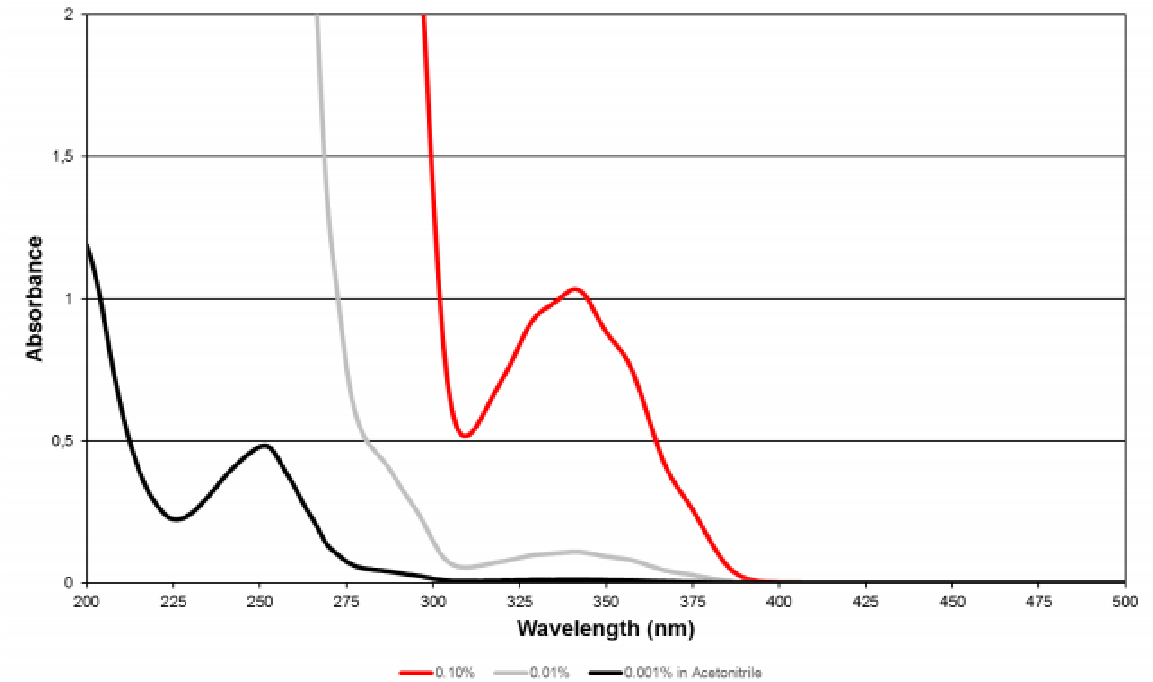

Figure C.1: Absorption for photoinitiator Omnirad BDK **source**

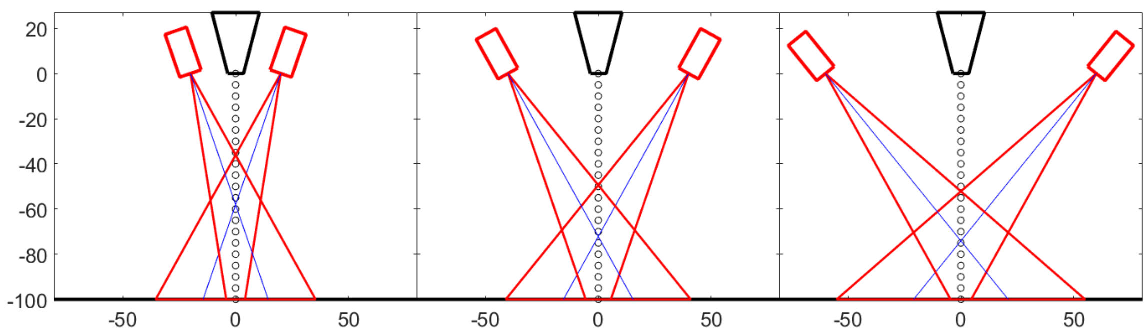

Figure C.2: Alternating the LED placement and angle with distance in mm

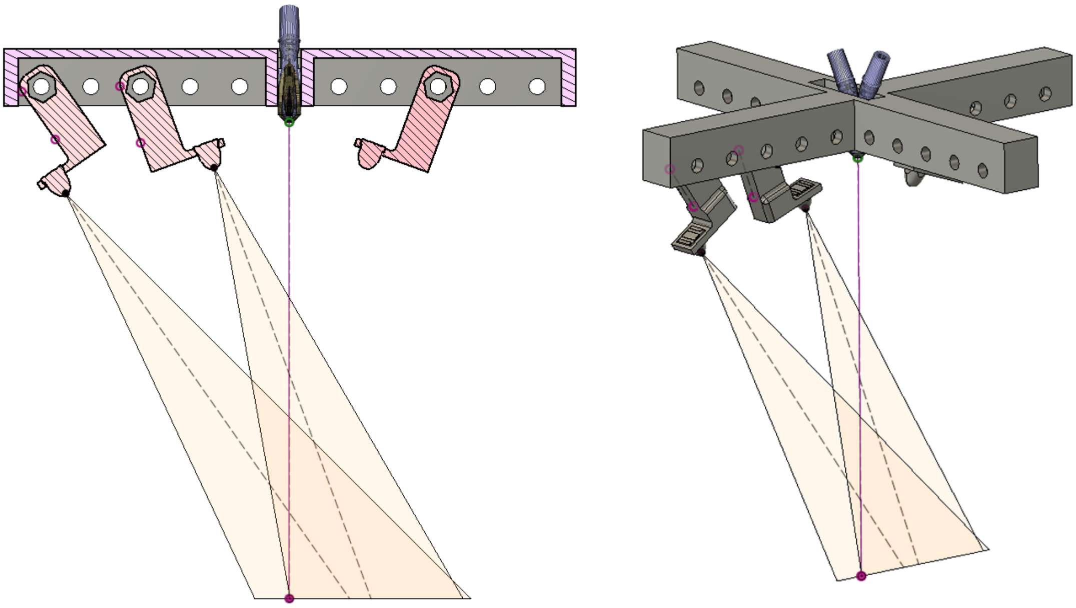

Figure C.3: Model of the array with a nozzle and three LEDs mounted